Robust Spin Control Design for the AOSAT+ Mission Concept

Ravi Teja Nallapu, Stephen R. Schwartz, Erik Asphaug, Jekanthan Thangavelautham

***Abstract*—The surfaces of asteroids are a challenging environment to explore due to their low gravity. Active small-body missions rely on short-duration touch-and-go operations to mitigate this risk. An in-depth understanding of the surface geophysics of asteroids and comets can open the door to prolonged surface and subsurface exploration of these small bodies. We propose the AOSAT+ mission concept, which will provide rich physics data of a simulated asteroid surface. The mission consists of a 12U CubeSat that will operate as a centrifuge laboratory in low Earth orbit (LEO). The CubeSat will carry 2.5 kg of crushed Allende meteorite, along with a suite of science instruments. The spacecraft will rotate at 0.1 to 1.1 RPM to simulate the milli-gravity environment of a desired small body. A major challenge with operating a centrifuging spacecraft is that it contains shifting masses, which result in perturbation torques on the spacecraft. This requires a robust attitude controller to spin the spacecraft at its target rotation speed. This work presents the development of a sliding mode attitude control law that enables the operation of the AOSAT+ Centrifuge mode. The perturbations of the regolith are modeled using a discrete element model (DEM), where the regolith grains are treated as inelastically colliding hard spheres. We begin by presenting a detailed overview of the AOSAT+ mission concept and its different operations. The regolith motion model implementation and the detailed derivation of the required sliding mode controller are then presented. The constraints presented by the actuators and tools to study their limitations are then developed. Finally, the controller is shown to successfully demonstrate the spin rate requirements of the AOSAT+ Centrifuge mode. Key insights on the operation of the Centrifuge mode, and important mission design considerations on the spacecraft are then noted.**

***Index Terms*—CubeSat Centrifuge, discrete element modeling (DEM), sliding mode controller, closed-loop reference tracking, spacecraft attitude control.**

I. Introduction

The surfaces of asteroids are challenging to explore due to a low gravity environment and the associated uncertainties. For this reason, active missions to asteroids such as OSIRIS-Rex [1] and Hayabusa-2 [2] rely on short duration touch and go operations which mitigates the risk. This is further complicated by the fact that there are a large number of asteroids known (about 2 million asteroids in the main belt), which exhibit a diverse set of physical characteristics, composition, and origin [3]. Despite these challenges, understanding asteroid surfaces can yield high-value science returns [4], and can also open new doors for prolonged exploration of the small bodies and the Solar System.

To address these challenges, we propose the AOSAT+ mission concept [5], which will simulate the surface of a desired asteroid inside a spacecraft in a low Earth orbit (LEO). —This can be used as an alternative to sending a spacecraft to explore an asteroid surface. The AOSAT+ spacecraft is a 12U CubeSat, which will carry 3 kg of crushed Allende meteorite. The surface generation is achieved by spinning the spacecraft about one of its fixed axes on its orbit. The concept of operations of the AOSAT+ mission is presented in Fig. 1. As seen here, after launch and deployment, the spacecraft will enter into a commissioning mode. In this mode, the spacecraft performs a detumble maneuver to nullify any angular velocities induced during deployment. Following this, the spacecraft will enter into its science mode, where the spacecraft will spin on one of its shorter body axes (body x-axis) in orbit. By the centrifugal action of the spacecraft, AOSAT+ will be able to simulate the surface gravity of a target body of interest. The requirement of the primary mission objective is that the attitude control system must be able to spin the spacecraft at speeds up to 1.1 RPM. The spacecraft will remain in the science mode for about 10 days spinning at different angular velocities between 0.1 RPM $-$ 1.1 RPM. After the 10 day period, the spacecraft will communicate its data to the Mobile CubeSat Command and Control (MC3) network of ground-stations operation by the Space Dynamics Laboratory [6]. These operations are cycled for about 1 year. These operations will enable AOSAT+ to meet its primary science objectives. After this, the spacecraft will operate in an extended science mode where the spacecraft will be commanded to spin at higher spin rates and active experiments such as impact strength measurement would be performed on the spinning regolith. While the science returns of the AOSAT+ are quite exciting, there are several interesting engineering challenges that need to be addressed for a successful implementation of the mission. This work will focus on developing control algorithms that meet the requirements of the AOSAT+ centrifuging operation.

This work addresses three challenges faced by the AOSAT+ spacecraft. The first challenge is that once the regolith is released into the science chamber, the moment of inertia of the total spacecraft will be fluctuating. Therefore, the attitude control law used must be able to compensate for this fluctuation. The second challenge is during the Centrifuge mode/ Science mode. Since most spacecraft missions have common operations such as Detumbling, Tracking, etc., these operations are typically preprogrammed by the vendors on board the off-the-shelf attitude control system. However, the centrifuge operation of AOSAT+ is not a common CubeSat operation mode and therefore the reference and control commands will be developed by the AOSAT+ engineering team at the University of Arizona. Additionally, due to their small size, the control envelopes of the attitude actuator are

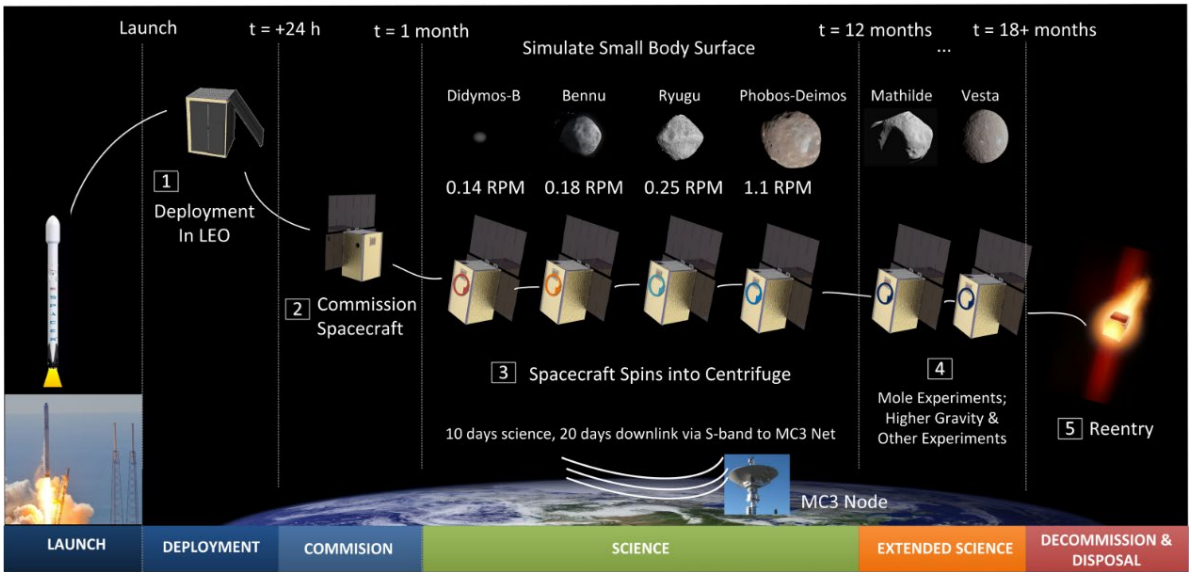

Fig. 1. The Concept of Operations of the AOSAT+ mission concept.

limited, therefore any control laws used should be inside the control envelope of the actuators.

In the present work, we develop a framework for modeling and controlling the Centrifuge mode of AOSAT+ using numerical simulations when subjected to the above-mentioned challenges. In this work, we model the perturbations arising from regolith using a discrete element methodology (DEM) where the particles are modeled as inelastically colliding hard spheres. We then develop a robust sliding mode controller to track the desired Centrifuge mode spin rate of AOSAT+. Finally, the constraints imposed by the selected attitude control actuators are then studied in order to understand the spacecraft capabilities.

The organization this work is as follows: Section II presents relevant work done in the micro-gravity simulations for space applications, and related attitude control problems. Section III describes the AOSAT+ spacecraft and its mission operations. Section IV describes the regolith motion model through hard sphere collisions. Following this, the sliding mode control law, which compensates for the inertia fluctuations, and parameter uncertainties, is derived in Section V. Here we present the requirements of the Centrifuge mode and develop the sliding mode control law for tracking a reference spin rate. The implementation of the control law using actuator saturation and analysis tools to study the performance bounds of the actuator are also presented here. Section VI describes the results of the numerical experiments of the AOSAT+ Centrifuge mode, where the sliding mode control algorithm is demonstrated. This is achieved by studying the controller performance on multiple regolith pools each with a different number of particles. Additionally, a thorough analysis of the controller performance and implications from actuator constraints is presented here. Finally, Section VII concludes the work by presenting a brief summary followed by identifying the pathways forward for the AOSAT+ mission concept.

II. Related Work

Simulating asteroid surface conditions remains a formidable challenge. The challenge comes from simulating the low-gravity conditions. Conventional methods of generating low-gravity conditions include parabolic flights [7], neutral buoyancy water tanks [8], and drop towers [9]. These methods simulate the required low gravity conditions either for a brief period, or present artifacts that cannot directly be correlated to that of asteroid surface conditions. A space-based centrifuge, on the other hand, appears to be a promising platform to simulate these low gravity conditions [10]. Space-based centrifuges have tested onboard the International Space Station (ISS) as a platform for several fundamental and biological experiments [11]. While ISS based centrifuges do offer a stable low-gravity platform, the random perturbative accelerations injected by the ISS subsystems [12] are comparable to the smallest target microgravity conditions of our experiments (10^{-5} g). This coupled with the low-cost feasibility and rapid miniaturization of CubeSat technologies [13] suggests that a dedicated orbiting CubeSat centrifuge as an ideal platform for our experiments.

Our first CubeSat centrifuge laboratory mission is called Asteroid Origins Satellite-1 (AOSAT-1) [14, 15]. The spacecraft is a 3U CubeSat, with the science chamber spanning two units (2U) of volume. This design provided an estimated moment arm of 20 cm. The Centrifuge mode of the AOSAT-1 mission requires that the spacecraft be spun at a constant 1 RPM, about its long axis, thus generating a peak centrifugal acceleration of 2.23×10^{-4} g ($1\,\mathrm{g} = 9.81 \frac{\mathrm{m}}{s^2}$), which is indicative of the gravity of sub a 1 km diameter asteroid [16]. The spacecraft will use a combination of reaction wheels and magnetorquers to achieve this attitude mode [17]. In comparison, the AOSAT+ is a larger spacecraft with a 12U CubeSat form factor [18]. The top 4U portion of the CubeSat spans the spacecraft avionics, while the remaining 8U spans the

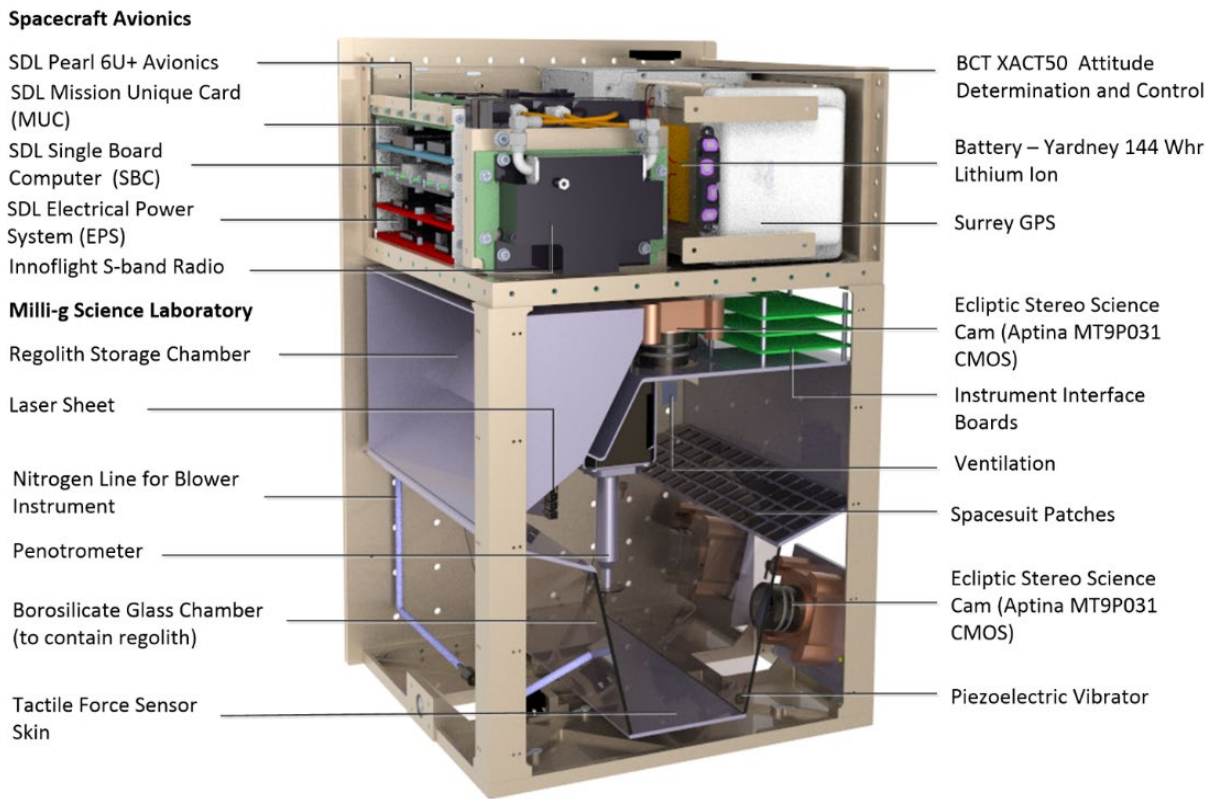

Fig. 2. CAD Assembly of the AOSAT+ spacecraft showing avionics and geoscience payload.

instruments, spin chamber, and the regolith required for the experiments as shown in Fig. 4. Despite similar moment arm lengths, AOSAT+ will be spun at multiple spin rates when compared to AOSAT-1, thus enabling it to generate the conditions of multiple target bodies as shown in Fig. 1. Additionally, the payload chamber will be equipped with multiple sensors and instruments facilitating a deeper study of the regolith dynamics inside the payload chamber.

Traditionally, the motion of regolith particles has been studied using the discrete element modeling (DEM) methodology [18, 19], where particles are treated as discrete entities that move due to mutual interactions such as collisions [20]. The hard sphere models are one of the modeling techniques of the DEM methodology where the particles are simulated as spheres that retain their shape after collisions [21]. The hard sphere models have been used to model the granular dynamics of asteroid regolith particles, where collision parameters such as the coefficient of restitution have been determined [22].

The primary focus of the current work is to develop and demonstrate a robust attitude control law for the Centrifuge mode of AOSAT+, under the presence of perturbations arising from moving regolith particles. The attitude dynamics and control of spinning spacecraft is well studied in the literature and several representations to study spacecraft attitude have been developed [23, 24]. The modified Rodriguez parameters (MRPs) [25] are one of the many convenient ways to represent spacecraft attitude as they form a minimal set representation [24] of the spacecraft attitude. Several spin-stabilized spacecraft, where a principal axis spin is used to regulate the attitude of the spacecraft, have been successfully flown [26]. The primary challenge to a spinning spacecraft comes from fluctuations in the net moment of inertia tensor of the spacecraft [27]. Important sources of such fluctuations arise from moving components such as fuel slosh [28, 29], solar panel deployment [30], and solar panel flexing [31]. The fuel sloshing is a phenomenon that occurs when a spacecraft carrying fuel is subjected to large maneuvers. Existing studies model the slosh as an oscillating pendulum and describe the perturbation due to the slosh as a dissipating energy function [32]. The solar panel deployment of a satellite takes place during the initial phase of the mission when its initially stowed solar panels are expanded to increase the Solar power input to the spacecraft. Since AOSAT+, similar to many small spacecraft, has a one-time solar panel deployment mechanism, this will not be a repeating source of perturbations. The solar-panel flexing, on the other hand, is due to the structural vibrations of the solar panels. While this is indeed a major source of perturbation for large spacecraft, the current work does not include the solar panel flexing because of the small spacecraft form factor of the spacecraft. It should be noted here that while the inertia fluctuations due to moving regolith are similar to the fluctuations arising from fuel slosh, the key difference lies in the fact that slosh results from the fluidic motion of the fuel, while the regolith motion is primarily dominated by the particle dynamics, and their collisions.

When such uncertainties are involved, nonlinear control theory offers two strategies to develop stable control laws: robust

control and adaptive control [33]. The robust control strategy contains a nominal control effort assuming a deterministic model, and a robust control effort to compensate for the system uncertainties. Adaptive control, in comparison, estimates the model at every instant and computes a control torque based on this model. The current work designs a sliding mode controller (SMC), which is one class of robust controllers. The SMC ensures the phase space of the dynamics converges to a designed manifold within a finite time. In the existing state of the art literature, sliding mode control laws have been designed and demonstrated to track time-varying reference attitudes [34, 35, 36]. While the design methodology of obtaining an SMC is well studied, designing a sliding mode controller to track a reference spin in the presence of fluctuating spacecraft inertia can be nontrivial as presented in the current work.

Our previous work on CubeSat based centrifuges focused on designing an attitude control law for AOSAT-1 [14, 17]. However, in this work, the regolith fluctuation was modeled as a random disturbance torque, and the stability of the controller was not discussed. Some of our recent efforts focused on modeling the high-fidelity dynamics of regolith [5, 37] using an N-particle tree code known as PKDGRAV [38]. Here, the motion of regolith inside the payload chamber was modeled by about 10^5 hard spheres of uniformly distributed diameters, when the payload chamber was subject to different target spin rates highlighted by the mission. The current work aims to apply the results obtained from Schwartz et al [37] to design a stable controller for the Centrifuge mode. Specifically, we model the spacecraft whose payload chamber contains particulate regolith inducing the perturbations. We then design a sliding mode controller which tracks a reference spin rate in presence of these perturbations.

III. Baseline Spacecraft and Mission Operations

This section presents a detailed overview of the AOSAT+ spacecraft and its mission operations. We begin with a description of the spacecraft subsystems followed by the different mission modes of the spacecraft. These modes correspond to the different attitude maneuvers required by the AOSAT+ mission.

A. Avionics

As mentioned in the previous section, the AOSAT+ spacecraft is a 12U CubeSat which has a total estimated mass of 24 kg, of which the regolith carried is about 3 kg. Fig. 2 shows a computer-aided design (CAD) representation of the AOSAT+ spacecraft assembly. The 12U bus will be developed by the Space Dynamics Laboratory (SDL). The design provides an estimated mass margin of 25% and volume margins of 44% [5]. The spacecraft uses an SDL built Single Board Computer containing Cobham Leon 3FT rad-hardened processor operating at 125 MHz coupled with a rad-tolerant Micro-semi FPGA, 256 Mb of SDRAM and 16 GB solid-state drive. The SBC board interfaces to the Mission Unique Card (MUC) via SpaceWire. The MUC hosts all the science instruments. The spacecraft will use the Innoflight SCR-101 S-band Radio capable of 1.5 Mbps data rate. The system is designed to send/receive at least 8bit tone data with a 6 dB margin even if the spacecraft is spinning. The SDL will be providing spacecraft tracking and communication services using the MC3 communications network.

B. Attitude Determination and Control System

The AOSAT+ uses the XACT 50 module from Blue Canyon Technologies to monitor and control its attitude. The architecture of the ADCS unit of AOSAT+ is presented in Fig. 3. This subsection presents the capabilities of the XACT 50 module.

Attitude Determination System. The attitude determination system (ADS) of the XACT 50 unit uses a star tracker; an IMU which comprises of a MEMS gyroscope, a magnetometer, and an accelerometer; and a Sun sensor. The XACT 50 unit runs a pre-programmed Kalman filter [39] attitude estimation algorithm with an estimated $1-\sigma$ pointing accuracies in the range of $0.003-0.007$ deg on all 3 axes. It is pointed out here that the accuracy of the attitude determination is expected to decrease during the centrifuge mode, especially while centrifuging at the maximum target rotation rates. However, during this mode spacecraft pointing will not be of concern, since the spacecraft will be sufficiently charged and prior to entering.

Attitude Control System. The attitude control system (ACS) of the XACT 50 unit uses reaction wheels and magnetorquers on all 3 axes. The XACT 50 unit uses a set of three RWp050 reaction wheels placed along 3 mutually perpendicular axes. Each reaction wheel has an estimated mass of 0.24 kg and a diameter of 5.8 cm. The reaction wheels can spin at a maximum speed of about 4731 RPM, to account for maximum angular momentum storage of 0.05 Nms. The reaction wheels can produce a maximum control torque of 0.007 Nm. The magnetorquers of the XACT 50 module have a maximum control dipole of 0.2 Am^2. The ADCS unit will be provided with preprogrammed operations such as spacecraft detumbling, pointing, and reaction wheel desaturation.

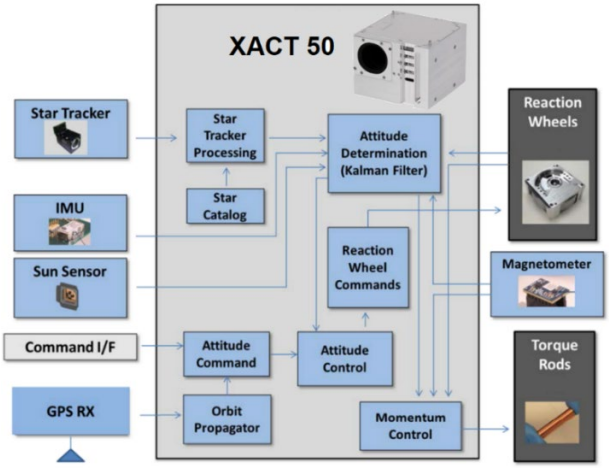

Fig. 3. The hardware architecture of the XACT 50 module, the selected ADCS unit of AOSAT+.

C. *Milli-g Science Lab Chamber*

The payload containing the spin chamber, and the sensor suite will be referred to as the milli − g science lab chamber. As seen in Fig. 2, the lab chamber spans the lower 8U volume of the to maximize the moment arm of the spacecraft spin. The regolith will initially be stored in the regolith storage chamber which is from the borosilicate glass chamber by a door mechanism. The door will be controlled by a burn-wire release mechanism. Upon triggering this during the start of the first science mode, the door drops, and the regolith comes out into the glass chamber aided by centrifugal. The glass chamber contains spacesuit material coupons, tactile force sensors, optical cameras. The force sensors will be placed at the bottom end of the lab chamber as shown in Fig. 2, where the maximum moment-arm inside the lab chamber can be experienced during the Centrifuge mode. Additionally, two stereo camera pairs consisting of four Aptina MT9P031 CMOS cameras will image and record the regolith during the experiments [5].

Regolith. A pool of asteroid regolith is flown inside the spacecraft which is produced by fragmenting 2.5 kg of a meteorite into a size distribution from 1 mm to 10 mm. We use the carbonaceous chondrite Allende, whose parent body may have been compositionally similar to our science targets, with which we have worked extensively. Numerical simulations of regolith dynamics indicate that the pool will be spanned by 9×10^4 - 1×10^5 regolith particles [37].

D. *Power System*

The spacecraft will be powered using two large body-mounted deployable MMA eHawk solar panels containing triple-junction cells. The eHawk configuration will avoid gimbaling in order to simplify the spacecraft operation. The system will charge a bank of 144 Whr Yardney Lithium-Ion batteries. The depth of discharge will not exceed 20 % to maximize battery capacity and life. Preliminary power budget analysis suggests a 25 % power margin [5].

E. *Spacecraft Configurations and Reference Frames*

As a result of solar panel deployment, the AOSAT+ spacecraft will essentially operate in two structural configurations. The first configuration will have stowed solar panels. After the initial detumbling, the spacecraft will deploy its solar panels and enter its second configuration. This deployment will cause the spacecraft to change its dynamic parameters such as the center of gravity, and the moment of inertia. Consequently, the motion of the spacecraft will be expressed in different reference frames. The spacecraft motion of interest to the current work is its attitude dynamics. The two configurations and their corresponding reference frames are depicted in Fig. 4. The reference frames used to describe the spacecraft attitude in both these cases are defined as follows:

Origin. The origins of the body frames in both configurations are located at their corresponding center of mass.

z-axis. The z-axis of both configurations will point downwards along the length of the spacecraft.

x-axis. In the stowed configuration, the x-axis will point along a direction parallel to the plane of the solar panels after their deployment. Once the panels are deployed, the stowed configuration reference frame will be rotated by a 90 deg counterclockwise rotation along its z-axis, which results in an x-axis which points normally outward from the plane of the deployed solar panels as shown in Fig. 4.

y-axis. The completes is defined using the right-hand rule over the x and z axes.

The left superscripts B_S, and B_D the body frame in the stowed and deployed configurations respectively. The frames are so defined in order to arrange the body frame principal moments of inertia along the $x, y,$ and z axes—J_x, J_y, and J_z-- will be sorted in the descending order convention, i.e., $J_x \geq J_y \geq J_z$, in both the coordinate frames [24]. In addition, the regolith motion also causes a change in the moment of inertia as described in Section IV. The regolith deployment occurs after the solar panels are deployed and before the spacecraft is ready to enter its first centrifuge operation. For this reason, in the deployed configuration, we note two types of inertia tensors. The first is when the solar panels are deployed, and the regolith is tightly stowed inside the storage chamber. The second parameter is the inertia only arising due to the stationary parts of the spacecraft, which corresponds to all subsystems except the regolith particles. This parameter is useful for modeling the centrifuge of the spacecraft, where the inertia due to the regolith is superimposed using a three-dimensional parallel axis theorem [24].

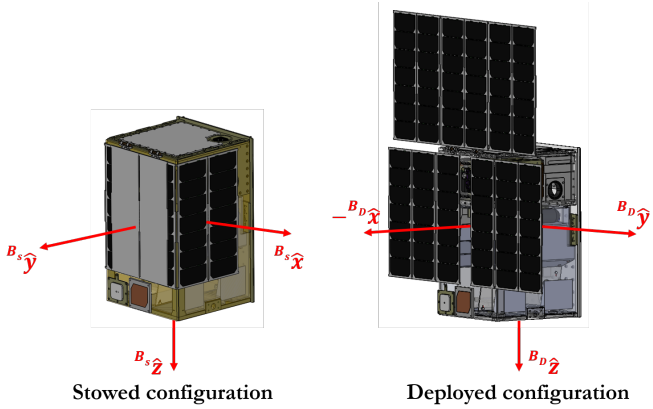

Fig. 4. The two structural configurations of AOSAT+, and their corresponding body frames. The origin of both frames is located at their corresponding center of mass.

Additionally, the CAD model indicates that the maximum moment arm from the spacecraft center of mass to the center of the chamber edge will be about 23 cm when no regolith is present inside the spacecraft. The structural parameters of the AOSAT+ spacecraft in the deployed configuration are summarized in Table 1.

F. *Baseline Orbit Parameters*

A low-Earth orbit was selected for AOSAT+ such that the access to the MC3 ground-station network was sufficient to meet the link margin requirements of the mission. The orbital

elements of the selected AOSAT+ orbit are listed in Table 2. The baseline orbit is used to define an instantaneous spacecraft reference frame, depicted in Fig. 5, in order to define the attitude. The origin and the basis vectors of the spacecraft presented are defined as follows:

Table 1. Dynamical parameters of the spacecraft in the deployed configuration.

Parameter	Value
Fixed spacecraft mass m_w, (kg)	20
Mass of regolith m_r, (kg)	2.5
Nominal max. moment arm length, r_c (cm)	23.0
Moment of inertia due to the fixed mass J_{ch}, (kg m^2)	$\begin{bmatrix} 0.343 & 0 & 0 \\ 0 & 0.224 & 0.01 \\ 0 & 0.01 & 0.326 \end{bmatrix}$

Origin. The origin of the orbit frame coincides with the spacecraft center of mass.

y-axis. The y-axis points along the direction of the spacecraft velocity with respect to the Earth-centered inertial J2000 reference frame N [40].

z-axis. The z-axis points towards the center of the Earth.

x-axis. The x-axis is defined by using the right-hand rule over the y and z axes.

A left superscript O beside a vector is used to indicate that the vector is resolved in the Orbital frame. The attitude maneuvers, of interest, in the current work, will be the orientation of the spacecraft body frames relative to the orbit reference frame.

Table 2. Orbital elements of the selected orbit for the AOSAT+ spacecraft.

Orbital Element	Value
Semi-major axis	6,928 km
Eccentricity	0
Inclination	43 deg
RAAN	90 deg
Argument of periapsis	0 deg

G. Mission Modes

After its deployment in the baseline orbit, the AOSAT+ spacecraft will start executing its mission operations. The operations are categorized into a set of spacecraft attitude modes. From an attitude control design perspective, the AOSAT+ spacecraft will have six modes of operation: Detumble, Panel deployment, Regolith deployment, Reference tracking, Desaturation modes, and Centrifuge modes.

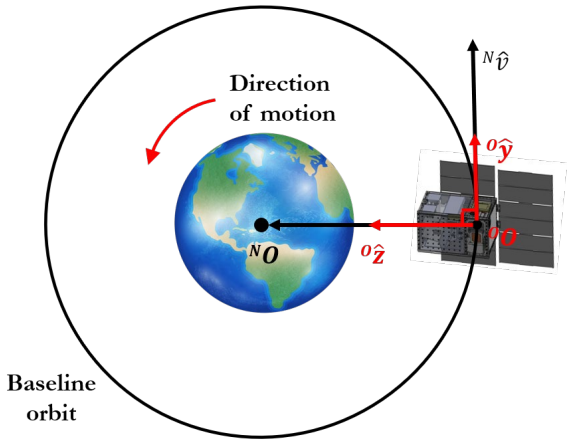

Fig. 5. The selected orbital frame of the spacecraft depicted in its orbital frame. The x-axis (not shown here) completes the right-hand triad and is along the outward normal direction to the orbital plane.

Detumble Mode. The Detumble mode occurs during the commissioning phase of the mission. The objective of this operation is to nullify any angular velocities on the spacecraft induced during deployment from the CubeSat dispenser. In this mode, the regolith is secured tightly in its storage chamber and the solar panels are in the stowed configuration. The spacecraft will use only the magnetorquers to regulate its angular velocity vector. At the end of this maneuver, the spacecraft will be able to begin its attitude acquisition.

Panel Deployment Mode. Once the spacecraft finishes its attitude acquisition, The AOSAT+ spacecraft will deploy its solar panels. During this operation, the spacecraft changes between its two structural configurations shown in Fig. 4. The attitude control system will ensure that this deployment does not cause the spacecraft to tumble.

Regolith Deployment Mode. Before beginning its experiments, the regolith stored inside the storage chamber will be allowed to enter into the science lab chamber. As mentioned above, the entry of the regolith into the chamber is blocked by a trapdoor which is secured by a burn wire mechanism. Upon a trigger, the locking wire is burnt, and the regolith now flows into the laboratory. This passage causes the inertia of the spacecraft to fluctuate. Similar to the Panel deployment mode, the attitude control system ensures that the spacecraft does not tumble during the regolith deployment.

Tracking Mode. A typical space mission requires its spacecraft to track a certain reference trajectory. This could be a rest-to-rest maneuver such as reorienting the spacecraft after a detumbling operation or enabling the appropriate subsystems to track time-varying vectors such as the ground station or the Sun. It is pointed here that since the AOSAT+ configuration varies with the deployment of solar panels and the regolith; each configuration will use a separate Tracking mode.

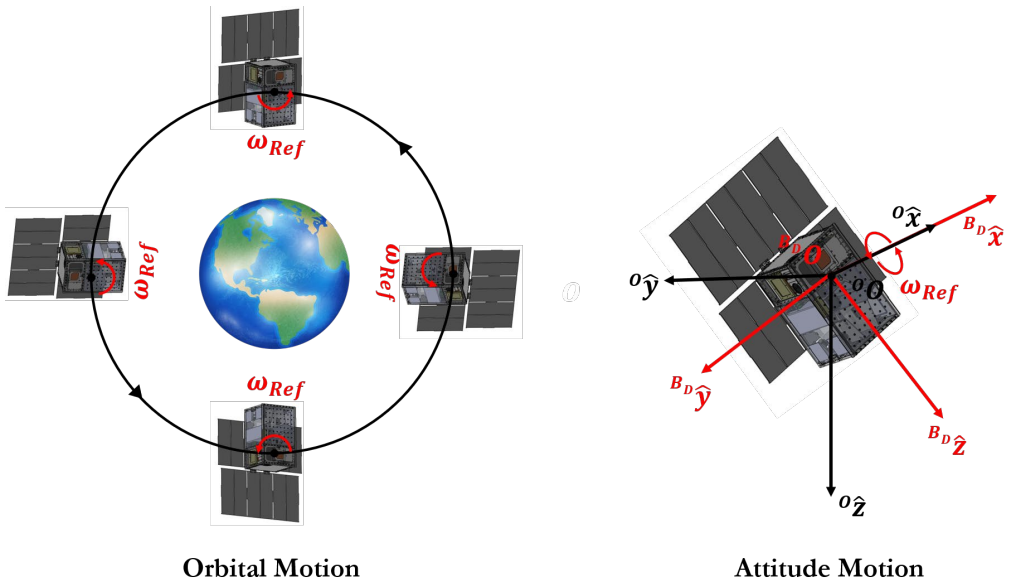

Fig. 6. Illustration of the Centrifuge mode of AOSAT+ showing the orbital motion of the spacecraft (left) and attitude motion profile (right).

Desaturation Mode. The Desaturation mode is responsible for dissipating the angular momentum built up in the reaction wheels over a long period of time due to the disturbance torques acting on the spacecraft. In this mode, the spacecraft uses its magnetorquers to dissipate the angular momentum of the wheels.

The five modes described here are a general characteristic of most spacecraft missions as they primarily require that the spacecraft does not tumble, or that the spacecraft be oriented along a particular direction with respect to the orbital frame. As a result, the controllers for these operations will be available as pre-programmed operations into the ADCS unit. The science mode, on the other hand, is a mission-specific operation, which requires a custom-developed controller.

H. Centrifuge Mode

The centrifuge operation forms the core of all the experiments planned by AOSAT+. In this mode, the spacecraft will be commanded to enter a counterclockwise spin of magnitude ω_{Ref} about the orbit frame x-axis as illustrated in Fig. 6. The rotations will produce a radially outward centrifugal acceleration on the regolith particles whose magnitude is given by

$$a_c = r_c \omega_{Ref}^2 \quad (1)$$

For a selected spin rate ω_{Ref}, the centrifugal acceleration will increase with increasing radial length, as observed from Equation 1, and inside the lab chamber of the AOSAT+ spacecraft, this will be maximum at the bottom end of the glass chamber where the tactile force sensors will be placed. The objective of the Centrifuge mode is to subject the regolith particles at the bottom end of the lab chamber to a centrifugal acceleration corresponding to a selected small body gravity regime by spinning at a target angular velocity. Thus, by selecting an appropriate spin rate ω_{Ref}, a centrifugal acceleration which is equivalent to an asteroid surface gravity level can be imparted onto the regolith particles at the end of the glass chamber. During its science phase, the spacecraft will aim to simulate the gravity regimes of four different small bodies in the Solar system [5] at the end of its glass chamber, by spinning at four different spin-rates as shown in Fig. 6. The different spin rates and target bodies are summarized in Table 3. The radial moment arm used in the computation of the centrifugal acceleration is noted from Table 1.

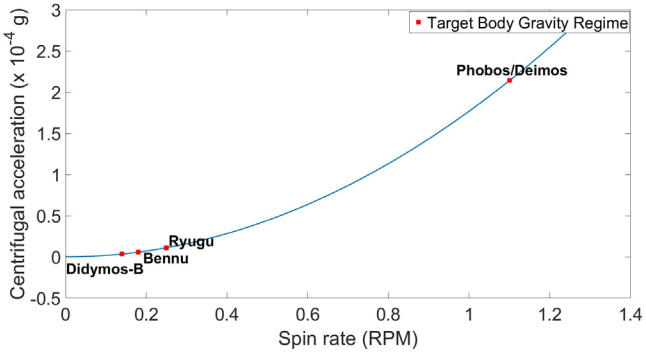

Fig. 7. The small body gravity regimes targeted by the Centrifuge mode of AOSAT+, along with the required spacecraft spin magnitude.

It should be noted here that the particles inside the chamber will be affected by other accelerations and perturbations, and that the centrifugal acceleration experienced by the regolith particles will vary based on its radial distance to the center of gravity. However, the insights from these experiments are still sufficient to meet the science objectives of AOSAT+ [5].

IV. Regolith Motion Model

In this section, we develop a numerical model of the motion of the regolith particles, and their perturbations to the spacecraft attitude dynamics. Here we assume that the particles are N hard

spheres that undergo inelastic collisions inside the spacecraft laboratory chamber.

Table 3. Reference spin parameters and target small bodies during the AOSAT+ Centrifuge mode.

Target Body	Spin rate (RPM)	Centrifugal Acceleration ($\times 10^{-4}$g)
Didymos-B	0.14	0.050
Bennu	0.18	0.083
Ryugu	0.25	0.160
Phobos/ Deimos	1.1	3.11

Additionally, we assume that the particles have no external forces and are purely under the ballistic regime. While such assumptions do not really hold true for the actual regolith grains, they provide faster computational performance. One major reason for this is the number of parameters required to specify the location of the sphere: specifying the location of the center, and its radius is sufficient to specify the location of a particle in a three-dimension space, while any other shape also requires the determination of the attitude of the particle. Hard sphere models have been widely used to model particle motion where computationally faster results have been preferred at the expense of losing certain realism [36, 37]. We begin by modeling the dynamics of the regolith particles as seen by the spacecraft body frame and then proceed to model the perturbations arising from the regolith collisions.

A. Regolith Motion

Consider an isolated spherical regolith particle of mass m_i, and radius α_i located inside the AOSAT+ spacecraft undergoing ballistic motion, as shown in Fig. 8. Let the particle have a position vector $\bar{r}_i$, and a velocity vector $\bar{v}_i$ with respect to the spacecraft body frame.

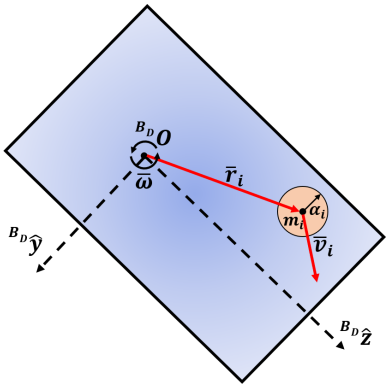

Fig. 8. Illustration of the particle motion inside the spacecraft frame.

Let the spacecraft be rotating with an angular velocity $\bar{\omega}$, with respect to the orbit frame described in Section III. Since the regolith particle has no net forces, the ballistic equations of the particle motion, describing the rate of change of position and velocity with respect to the rotating body frame of the spacecraft can be expressed as [20]:

$$\dot{\bar{r}}_i = \bar{v}_i \tag{2}$$

and

$$\dot{\bar{v}}_i = -(\bar{\omega} \times \bar{\omega} \times \bar{r}_i) - 2(\bar{\omega} \times \dot{\bar{r}}_i) - (\dot{\bar{\omega}} \times \bar{r}_i) \tag{3}$$

The particle will continue to undergo the motion described by the differential equations presented in Equations 2 and 3 until its trajectory is changed due to colliding with either other particles, or the boundaries of the laboratory chamber. In order to facilitate a simplistic treatment, we only consider the effects of binary collisions, where only collisions of two particles are checked at a given time. We will now proceed to describe the models for collision checks, and post-collision velocities used in the current work.

B. Particle-Particle Collisions

The binary particle-particle collisions will occur when the distances between the particles below the sum of their radii as described by Equation 4. Consider two particles, whose indices are specified by $i = p$, and q, move on a collision course as shown in Fig. 9. Let the collision occur at a time instant t when the particles are located at $\bar{r}_p(t)$ and $\bar{r}_q(t)$, and have velocities $\bar{v}_p(t)$ and $\bar{v}_q(t)$ respectively.

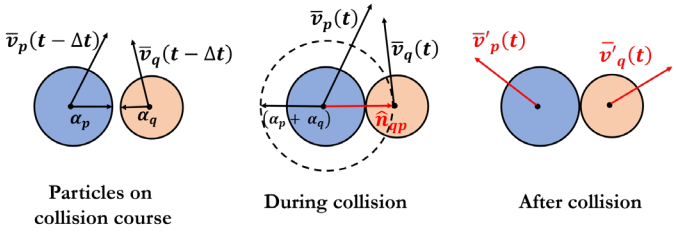

Fig. 9. Collision geometry during a particle-particle collision.

These position and velocity vectors are expressed in the deployed AOSAT+ body frames as described in Fig. 4 and Fig. 8. The two colliding particles will then satisfy the condition:

$$\left|\bar{r}_p(t) - \bar{r}_q(t)\right| \leq \alpha_p + \alpha_q \tag{4}$$

The objective is then to determine the modified velocities of the particles after the collision. The normal impulse imparted on these spherical particles can be written as [38]:

$$J_{qp,n} = -\frac{m_p m_q (1 + C_r)}{m_p + m_q}\left(\bar{v}_q(t) - \bar{v}_p(t)\right).\hat{n}_{qp} \tag{5}$$

Where, $\hat{n}_{qp}$ is the unit vector from sphere p to sphere q as shown in Fig. 9., and C_r is the coefficient of restitution between the two collisions. The post-collision velocities of particles are noted as

$$\bar{v}'_p(t) = \bar{v}_p(t) - \frac{J_{qp,n}}{m_p}\hat{n}_{qp}$$

$$\bar{v}'_q(t) = \bar{v}_q(t) + \frac{J_{qp,n}}{m_q}\hat{n}_{qp} \quad (6)$$

The particle velocities computed using Equations 6 are applied to propagate the particle motions by solving the differential equations presented in Equations 2 and 3. This process is looped throughout the simulation timespan. Additionally, in order to prevent particle, overlap the particle positions are reset [39] after a collision as

$$\bar{r}'_p(t) = \bar{r}_p(t) - \alpha_p\hat{n}_{qp}$$

$$\bar{r}'_q(t) = \bar{r}_p(t) + \alpha_q\hat{n}_{qp} \quad (7)$$

C. Particle-Boundary Collisions

Collisions with the particle boundary also influence the particle motion. In addition, these will also influence the spacecraft dynamics. These collisions of the boundary will perturb the moment of inertia thus imparting disturbance torques on the spacecraft. Consider a particle i on a collision course with the chassis boundary wall as shown in Fig. 10. A check to determine if the particle has collided with the walls of the chamber can be described based on its cartesian coordinates as:

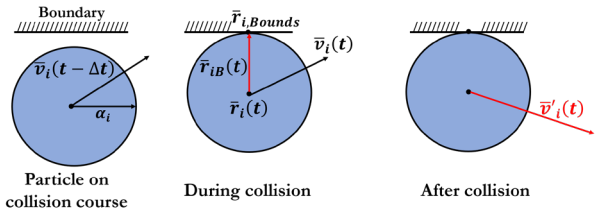

Fig. 10. Collision geometry during a particle-boundary collision.

$$\text{abs}(\bar{r}_{iB})_j = \text{abs}\left(r_{i_j} - j_{bound}\right) \leq \alpha_i \quad (8)$$

Where r_{i_j} is the j^{th} component of vector $\bar{r}_i$, and j_{bound} denotes both the upper and lower cartesian components along the dimension j. If a collision is detected with a face along the dimension j_c, the position of the particle reset in order to prevent particles from escaping the boundary as

$$r'_{i_j} = j_{c,bound} \pm \alpha_i \quad (9)$$

The positive sign in Equation 9 corresponds to a collision with the face along the lower bound, and the negative sign corresponds to a collision with a face along the upper boundary. Since the motion of the particles is modeled in the spacecraft body frame, the chamber is assumed to be at rest during the collision. The normal impulse imparted during the collision, from Equation 5, can be expressed as

$$J_{wi,n} = \frac{m_w m_i(1+C_r)}{m_w + m_i}.\frac{(\bar{v}_i(t).\bar{r}_{iB})}{|\bar{r}_{iB}|} \quad (10)$$

Where, m_w is the fixed mass of the spacecraft listed in Table 1. The updated post-collision velocity of particle i can be now be expressed, similar to Equation 6 as:

$$\bar{v}'_i(t) = \bar{v}_i(t) - \frac{J_{wi,n}}{m_i}\frac{\bar{r}_{iB}}{|\bar{r}_{iB}|} \quad (11)$$

However, this will also cause a velocity perturbation on the walls of the chamber:

$$\bar{v}'_{w,i}(t) = \frac{J_{wi,n}}{m_w}\frac{\bar{r}_{iB}}{|\bar{r}_{iB}|} \quad (12)$$

It is pointed out here that the velocity imparted by particle i after collision $\bar{v}'_{w,i}(t)$, does indeed affect the spacecraft velocity with respect to the orbit frame in Fig. 5. However, since the current goal is to model the motion of regolith with respect to the spacecraft body frame, the velocity of the wall is always considered to be at rest before and during the collision.

D. Regolith Perturbation

During a simulated instant, if a set of particles collide with the boundary, they will become a contiguous part of the spacecraft structure at that instant. Additionally, particles that collide with these boundary particles also continue to become a part of the spacecraft structure and allow other colliding particles to do the same. If we denote the set of indices of all the particles that form a part of the spacecraft structure as S_p, the net change in the spacecraft inertia tensor can be modeled as by using a three-dimensional parallel axis theorem [20] as:

$$J_{sc} = J_{ch} + \sum_{i \in S_p} m_i\,[\tilde{\bar{r}}_i(t)][\tilde{\bar{r}}_i(t)]^T \quad (13)$$

Where, J_{ch} is the moment of inertia due to the fixed mass in Table 1, and the $[\tilde{\cdot}]$ operator denotes the conversion of the input vector into its skew-symmetric matrix form. A major challenge which is now presented: in order to evaluate Equation 11 is to determine the set of particles S_p that contribute to the spacecraft structure. In order to address this challenge, we flag each simulated particles using a flag parameter to specify if the particle falls inside S_p.

Structure Flags. A binary flag parameter is used to indicate if a simulated particle forms a contiguous volume with the spacecraft. At the start of the simulation timestep, all particles will be initialized to 0 indicating that none of the particles form a contiguous spacecraft structure. After initialization, all particles in the simulated pool are checked for particle-boundary collisions using Equation 8. If a particle i satisfies Equation 8, its corresponding structure flag SF_i is set to 1. This forms an initial set of particles that directly contribute to the spacecraft's structure. We then proceed to check for particle-particle collisions using Equation 4. If a binary collision contains a particle whose structure flag is 1, the flag corresponding to the partner will also be set to 1. Therefore, the post-collision structure flags of two colliding particles are set

using the binary-or operation on their pre-collision structure flags. An illustration of the application of the structure flag is presented in Fig. 11.

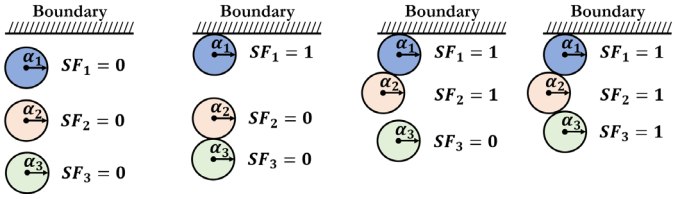

Fig. 11. Application of the structure flag parameter in order to determine whether a regolith particle will be considered as a part of the spacecraft structure.

At the end of a simulation timestep, all the particles whose structure flag is set to 1, will be included in the structure set S, therefore contributing the spacecraft inertia tensor as indicated by Equation 13. The algorithms presented here for modeling the motion of regolith are summarized in the pseudocode presented in Fig. 12. As presented here, we perform hierarchical collision checks between particle-pairs based on their indices. We note that such checks still contain the possibility that the collision flags of particles are not updated during a collision of multiple particles, depending on the order of the indices being checked. In order to randomize this effect, the primary particle is randomly sampled from the pool as indicated in Fig. 12. Another challenge that can be seen in Fig. 12. is that particle-particle collision model has an $O(N^2)$ complexity. While collisions of more than two particles are indeed a possibility in the real Centrifuge mode of AOSAT+, it drastically increases the computational complexity of the models. For this reason, the current work only limits the collisions to binary collisions. However, it should be mentioned here that due to the ordering of the collision checks presented in Fig. 12, binary collision effects of multiple particles colliding simultaneously are considered by the algorithm described here.

E. Centrifugal Acceleration

As a baseline to estimate the centrifugal accelerations experienced at the bottom of the laboratory chamber the centrifugal acceleration [20] is estimated as

$$(\bar{\omega} \times \bar{\omega} \times (\bar{r}_c - \bar{r}_{cm}(t))) \tag{14}$$

Where $\bar{r}_{cm}$ is the position vector of the center of mass of the spacecraft, and $\bar{r}_c$ is the moment arm vector. The center of mass of the spacecraft serves as the origin of the spacecraft body frame. However, the fluctuations of the regolith particles can cause an instantaneous shift in the center of mass at every simulation timestep. The shifted center of mass at every simulation timestep is then computed using the weighted average of the masses contributing to the spacecraft structure.

$$\bar{r}_{cm}(t) = \frac{\sum_{i \in S_p} m_i \bar{r}_i}{m_w + \sum_{i \in S_p} m_i} \tag{15}$$

The moment arm vector is the position vector from the nominal center of gravity to a point exactly below it (see Fig. 13), and is of the form

$$\bar{r}_c = \begin{bmatrix} 0 \\ 0 \\ r_c \end{bmatrix} \tag{16}$$

The length of the moment arm r_c can be noted from Table 1.

```
t = 0
Initialize: N particles inside the regolith chamber
Define:     Search order SO = {1:N − 1}
while t ≤ t_stop:
    Initialize: SF_i = 0  ∀ i ≤ N
    Shuffle:    elements in SO by randomly permuting its elements

    for i = 1:N                                                        ┐
        Check if particle i collides with boundary using Equation 8    │ Particle-boundary
        if collision occurs:                                           │ collisions
              Update: particle states using Equations 9 and 11         │
              Update: SF_i = 1                                         ┘

    for i in SO                                                        ┐
        for j = i + 1:N                                                │ Particle-particle
            Check collisions between particles i and j using Equation 4 │ collisions
            if collision occurs:                                       │
                Update: particle states using Equations 5 and 6        │
                Compute: F = (SF_i (binary-or) SF_j)                   │
                Update: SF_i = F and SF_j = F                          ┘

    Compute:    S = {All indices i, where SF_i = 1}
    Update:     spacecraft inertia J_sc using Equation 13
    Solve:      Equations 2 and 3 to compute: r̄_i(t + Δt) and v̄_i(t + Δt)   ∀ i ≤ N
    Solve:      Equations 18-25 to propagate spacecraft attitude motion
    t = t + Δt
```

Fig. 12. Pseudo-code illustrating the application of the algorithms used to model the motion of the regolith inside the simulated AOSAT+ laboratory.

F. Boundary Conditions

As seen in Fig. 2, the regolith containment chamber has a complex shape, whose width changes with the depth. Specifically, the width of the chamber x tapers with three different slopes based on the value of the depth z, while the value of y is nearly unchanged. We model the regolith chamber inside the post-deployment spacecraft body frame presented in Fig.4, using patches of linear approximations. If a particle p has a z coordinate z_p, and is inside a depth regime specified by $[z_{Bound,j-1},\ z_{Bound,j}]$, the boundary along the width dimension is specified as:

$$x_{Bound,j} = \pm \text{abs}\left(x_{Bound,j-1} - \tan\theta_j \left(z_P - z_{Bound,j-1}\right)\right)$$

when

$$z_{Bound,j-1} \leq z_P \leq z_{Bound,j} \tag{17}$$

Where, θ_j is the taper angle corresponding to depths between $[z_{Bound,j-1},\ z_{Bound,j}]$. The positive sign in Equation 17 corresponds to the upper bound while the negative sign corresponds to the value of the lower bound. The boundary along the length dimension y is defined by $[-y_{Bound},\ y_{Bound}]$. The bounds and slopes used, in the current work, to model the science laboratory are presented in Table 4. The simulated boundary of the AOSAT+ science with its various design elements is visualized in Fig. 13.

Table 4. Regolith containment chamber parameters.

Parameter	Value
$x_{Bound,0}$ (cm)	Upper bound: 10 Lower bound: -10
y_{Bound} (cm)	Upper bound: 11 Lower bound: -11
$z_{Bound,0}$ (cm)	3
θ_j (deg)	[0 40 30]
z_{Bound} (cm)	[7 11 23]

In the current work, the effect of regolith particles over the spacecraft motion is studied by simulating multiple regolith pools with a different number of particles N.

V. Attitude Dynamics and Control Design

This section presents an overview of the spacecraft attitude dynamics and the development of the sliding mode controller for the Centrifuge mode. Additionally, we also describe the constraints imposed by the spacecraft actuators on the Centrifuge mode of the spacecraft.

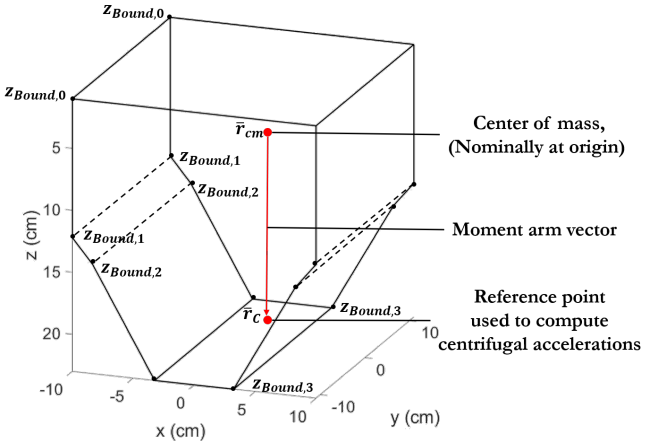

Fig. 13. The simulated AOSAT+ science laboratory key simulation parameters.

A. Attitude Dynamics

The primary interest here is the attitude of the spacecraft body frame with respect to its orbital frame. Let the attitude spacecraft body frame with respect to its orbit frame be denoted by the Modified Rodriguez Parameters (MRPs) $\bar{\boldsymbol{\sigma}}$ [25], with its vector components given by σ_x, σ_y, and σ_z, and magnitude is given by σ. Let $\bar{\omega}$ denote the angular velocity of the spacecraft body frame with respect to its orbit frame, and $\bar{\Omega}$ denote a 3×1 vector containing the angular velocities of the three reaction wheels onboard the spacecraft. The time evolution of the MRPs is governed by the following kinematic differential equation [20].

$$\dot{\bar{\boldsymbol{\sigma}}} = \frac{1}{4}[B(\bar{\boldsymbol{\sigma}})]\bar{\omega} \tag{18}$$

where the matrix function $[B(\bar{\boldsymbol{\sigma}})]$ is defined as

$$[B(\bar{\boldsymbol{\sigma}})] = (1 - \sigma^2)[I] + 2[\tilde{\boldsymbol{\sigma}}] + 2\bar{\boldsymbol{\sigma}}\bar{\boldsymbol{\sigma}}^{\boldsymbol{T}} \tag{19}$$

where $[I]$ is the 3×3 identity matrix. The evolution of MRP's periodically capped by switching to a shadow set in order to prevent controller unwinding using the relation

$$\bar{\boldsymbol{\sigma}} = -\frac{\bar{\boldsymbol{\sigma}}}{\sigma^2} \quad \text{if } \sigma > 1 \tag{20}$$

In order to derive the attitude dynamics which accounts for the inertia fluctuation, consider the spacecraft angular momentum [20] $\bar{H}$ given by

$$\bar{H} = [J]\bar{\omega} + [W_s]\bar{h}_s \tag{21}$$

Where, $[W_s]$ is the wheel alignment matrix whose columns denote the spin axes of the reaction wheels with respect to the spacecraft body frame, and $\bar{h}_s$ denotes the reaction wheel angular momentum, whose cartesian components are given by:

$$h_{s_i} = J_{s_i}(\Omega_i + \bar{\omega}.\hat{w}_{s_i}) \tag{22}$$

Where J_{s_i} is the moment of inertia of the reaction wheel along the i^{th} direction, and $\hat{w}_{s_i}$ is the i^{th} column of $[W_s]$. Differentiating Equation 21 using the transport theorem gives

$$\dot{\bar{H}} = \bar{\tau}_{ext} = [J]\dot{\bar{\omega}} + [\dot{J}]\bar{\omega} + [\tilde{\bar{\omega}}]([J]\bar{\omega} + [W_s]\bar{h}_s) - [W_s]\bar{U}_C \quad (23)$$

Where $\bar{\tau}_{ext}$ denotes the vector sum of any disturbance torques acting on the spacecraft, and $\bar{U}_{RW}$ is the reaction wheel control torque whose components are given by

$$U_i = -J_{s_i}(\dot{\Omega}_i + \dot{\bar{\omega}}.\hat{w}_{s_i}) \quad (24)$$

Additionally, Equation 24 can be solved for $\dot{\Omega}_i$ in order to describe the time evolution of the reaction wheel angular velocities. Equation 23 can now be rewritten to describe the evolution of the spacecraft angular velocities as

$$\dot{\bar{\omega}} = -[J]^{-1}([\tilde{\bar{\omega}}]([J]\bar{\omega} + [W_s]\bar{h}_s)) - [J]^{-1}[\dot{J}]\bar{\omega} + [J]^{-1}\bar{\tau}_{ext} + [J]^{-1}[W_s]\bar{U}_{RW} \quad (25)$$

It is noted here that Equation 25 is largely similar to the standard Euler's equation of attitude dynamics [20]. However, the standard form is now modified to also describe the effect of regolith fluctuations of the spacecraft attitude through the $[J]^{-1}[\dot{J}]\bar{\omega}$ term.

B. Robust Control Design

The Sliding mode control law is a robust non-linear controller [33] used in tracking control of systems with uncertainties. For AOSAT+, the regolith motion is the main source of uncertainty during the Centrifuge mode. For this reason, we develop a sliding mode control law for AOSAT+ to robustly track its reference attitude in the presence of inertia fluctuations and other parametric uncertainties. In order to derive the reference tracking sliding mode controller for AOSAT+, we revisit the sliding mode control design by Kowalchuk et. al. [36] and modify this to compensate for the inertia fluctuations. We begin by rewriting Equation 25 as

$$\dot{\bar{\omega}} = f + g\bar{U}_{RW} \quad (26)$$

Where,

$$f = -[J]^{-1}([\tilde{\bar{\omega}}]([J]\bar{\omega} + [W_s]\bar{h}_s) - [\dot{J}]\bar{\omega} + \bar{\tau}_{ext}) \quad (27)$$

and

$$g = [J]^{-1}[W_s] \quad (28)$$

Since f and g describe the true dynamics of the system which are not precisely known due to fluctuations and uncertainties, we model the dynamics using their approximations $\hat{f}$ and $\hat{g}$ respectively, i.e.,

$$\dot{\bar{\omega}} = \hat{f} + \hat{g}\bar{U}_{RW} \quad (29)$$

These approximations are selected by the control designer to nominally estimate the true dynamics. The assumption here is that we can estimate the bounds on these approximations as

$$\text{abs}(f - \hat{f}) \leq F \quad (30)$$

and

$$g = (I + \Delta_g)\hat{g} \quad (31)$$

Where the uncertainty Δ_g is bounded by $\Delta_g \leq D_g$. For the current work, we assume that the nominal dynamics are estimated using

$$\hat{f} = -[\hat{J}]^{-1}([\tilde{\bar{\omega}}]([\hat{J}]\bar{\omega} + [\widehat{W}_s]\bar{\hat{h}}_s)) \quad (32)$$

and

$$\hat{g} = [\hat{J}]^{-1}[\widehat{W}_s] \quad (33)$$

Where $[\hat{J}]$, $[\widehat{W}_s]$, and $\bar{\hat{h}}_s$, are nominal estimations of spacecraft moment of inertia, spin alignment matrix, and instantaneous reaction wheel angular momentum vector respectively. The uncertainties over these nominal estimations are also assumed to be bounded and will be discussed in subsequent sections. The objective of the robust control design problem then is to control a system which, in reality, is governed by Equation 26 while we can only model its nominal dynamics governed by Equation 29. Specifically, for the AOSAT+ Centrifuge mode, we require that the spacecraft's attitude be controlled to track a time-varying attitude $\bar{\boldsymbol{\sigma}}_{\boldsymbol{Ref}}$, with a fixed reference angular velocity $\bar{\omega}_{Ref}$ despite the inertia fluctuations and uncertainties.

Sliding Surface. We define a surface variable S given by

$$S = \delta\bar{\omega} + K_P\delta\bar{\boldsymbol{\sigma}} + K_I\int_0^t \delta\bar{\boldsymbol{\sigma}}\,dt \quad (34)$$

where, $\delta\bar{\omega}$ is the angular velocity difference given by

$$\delta\bar{\omega} = \bar{\omega} - \bar{\omega}_{Ref} \quad (35)$$

and $\delta\bar{\boldsymbol{\sigma}}$ is the MRP difference [20] given by

$$\delta\bar{\boldsymbol{\sigma}} = \frac{(1-\sigma_{Ref}^2)\bar{\boldsymbol{\sigma}} - (1-\sigma^2)\bar{\boldsymbol{\sigma}}_{\boldsymbol{Ref}} + 2\bar{\boldsymbol{\sigma}}\times\bar{\boldsymbol{\sigma}}_{\boldsymbol{Ref}}}{1+\sigma^2+\sigma_{Ref}^2 + 2\bar{\boldsymbol{\sigma}}.\bar{\boldsymbol{\sigma}}_{\boldsymbol{Ref}}} \quad (36)$$

The parameters K_P and K_I are diagonal matrices with positive elements on their diagonals that serve as control gains. The surface variable S is chosen such that the spacecraft tracks the reference attitude on the level surface given by the surface $S = 0$. Differentiating Equation 34 on the surface $S = 0$ and substituting Equation 26, leads to

$$\dot{S} = f + \Gamma + g\bar{U}_{RW} \quad (37)$$

where,

$$\Gamma = -\dot{\bar{\omega}}_{Ref} + [\tilde{\bar{\omega}}]\bar{\omega}_{Ref} + \frac{1}{4}K_P[B(\delta\bar{\boldsymbol{\sigma}})]\delta\bar{\omega} + K_I\delta\bar{\boldsymbol{\sigma}} \quad (38)$$

Setting $\dot{S} = 0$, allows us to synthesize a nominal control law given by

$$\bar{U}_{nom} = -\hat{g}^{-1}\left(\hat{f} + \Gamma\right) \quad (39)$$

In cases where $\hat{g}^{-1}$ does not exist, its pseudoinverse is traditionally used. Simply put, the nominal control torque ensures that once a spacecraft state ($\bar{\boldsymbol{\sigma}}$, $\bar{\omega}$) enters a point on the manifold $S = 0$, its time evolution always slides along this surface if the dynamics are governed by Equation 29. In addition to the nominal controller, a robust control term is also prescribed to ensure that the attitude evolution is maintained on the manifold in presence of the uncertainties. The Robust controller is of the form [36]

$$\bar{U}_{rob} = -K_S\,\mathrm{Sat}\left(\frac{S}{\Phi}\right) \quad (40)$$

where K_S is a positive sliding gain, and Sat(.) is the saturation function over two input vector arguments, which modifies the cartesian components of S as

$$\mathrm{Sat}\left(\frac{S_i}{\Phi_i}\right) = \mathrm{sign}(S_i) \quad \text{if } \mathrm{abs}(S_i) > \Phi_i$$

$$= S_i \quad \text{otherwise} \quad (41)$$

It is assumed here that all elements of the vector Φ are positive. The saturation function is used in place of the sign function to the avoid control chatter problem, which causes the controller to generate alternative positive and negative torques when the spacecraft state is relatively close to the manifold. The vector Φ describes this closeness to the manifold, where the controller is demanded to switch from the oscillating behavior of the sign function to a smoother linear function. The total control torque output desired from the reaction wheels for this robust control algorithm is now given by the sum of the nominal and robust components, i.e.,

$$\bar{U}_{RW} = \bar{U}_{nom} + \bar{U}_{rob} \quad (42)$$

Gain Selection. Examining Equations 35-37, it appears that the control design problem can be reduced to specifying the parameters K_P, K_I, and K_S. The gains K_P, K_I can be designed based on traditional control design methods such as trial and error, or to make the linearized nominal dynamics meet demand specifications such as peak overshoot and settling time requirements. The sliding gain, on the other hand, should be selected in order to compensate for the uncertainties. In order to achieve this, we define a candidate Lyapunov function [20]

$$V = \frac{1}{2}S.S \quad (43)$$

The function V is a positive definite function over S. In order to make the dynamics on S exponentially stable [33], we impose a condition such that

$$\dot{V} = \dot{S}^T.S \leq -\eta\,|S| \quad (44)$$

Which is known as the reachability condition. The parameter η is a vector with positive elements, which constraints the time of convergence to the reference trajectory. It can be shown that Equation 44 can be reduced to yield a lower bound on the sliding gain K_S as [36]

$$K_S \geq \left(I - D_g\right)^{-1}(F + \left|D_g\left(\hat{f} + \Gamma\right)\right| + \eta) \quad (45)$$

Equation 45 can be converted to equality to obtain an expression for the sliding gain. It can be noted from here that the sliding gain varies dynamically due to its dependence on F, $\hat{f}$, and Γ. The key point to note here is that the fixed control parameters of a sliding mode controller are the gains K_P and K_I; and the parameters η and Φ. The dynamic requirements on the sliding gain require the control designer to model the uncertainty bounds F and D_g, which will now be described.

Uncertainty Bounds. The uncertainty on dynamics F is placed by examining the difference $f - \hat{f}$, i.e.,

$$F \geq \Big|-[J]^{-1}\left([\tilde{\bar{\omega}}]\,([J]\bar{\omega} + [W_s]\bar{h}_s)\right) + [J]^{-1}\bar{\tau}_{ext}\,)$$

$$+ [\hat{J}]^{-1}\left([\tilde{\bar{\omega}}]\,([\hat{J}]\bar{\omega} + [\widehat{W}_s]\bar{\hat{h}}_s)\right) - [J]^{-1}[\dot{J}]\bar{\omega}\Big| \quad (46)$$

Let the uncertainty in the inertia matrix, and the uncertainty on reaction wheel angular momentum be given by

$$[J] = (I + \Delta_J)\,[\hat{J}] \quad (47)$$

and

$$[W_s]\bar{h}_s = (I + \Delta_h)\,[\widehat{W}_s]\bar{\hat{h}}_s \quad (48)$$

where $\Delta_J \leq \mathrm{D}_J$ and $\Delta_h \leq \mathrm{D}_h$. Taking the inverse of Equation 47, we get

$$[J]^{-1} = [\hat{J}]^{-1}(I + \Delta_J)^{-1} \quad (49)$$

Which is bounded using its first-order linear approximation as

$$[J]^{-1} \leq [\hat{J}]^{-1}(I + \Delta_J) \quad (50)$$

The terms in Equation 46 can be regrouped as

$$F_1 = \Big|-[J]^{-1}\left([\tilde{\bar{\omega}}]\,([J]\bar{\omega} + [W_s]\bar{h}_s)\right) + [J]^{-1}\bar{\tau}_{ext}\,)$$

$$+ [\hat{J}]^{-1}\left([\tilde{\bar{\omega}}]\,([\hat{J}]\bar{\omega} + [\widehat{W}_s]\bar{\hat{h}}_s)\right)\Big| \quad (51)$$

and

$$F_2 = \left|-[J]^{-1}[\dot{J}]\bar{\omega}\right| \quad (52)$$

As presented in Kowalchuk et. al. [36], the first term F_1 is bounded by

$$F_{1,UB} = [\hat{J}]^{-1}\left|(D_J[\tilde{\bar{\omega}}] - [\tilde{\bar{\omega}}]D_J + (D_J[\tilde{\bar{\omega}}]D_J)[\hat{J}]\bar{\omega} + (D_J[\tilde{\bar{\omega}}] - [\tilde{\bar{\omega}}]\mathrm{D}_h + (D_J[\tilde{\bar{\omega}}]D_h)D_s\right| + [\hat{J}]^{-1}(D_J + I)\bar{\tau}_{max} \quad (53)$$

Where D_s is the maximum uncertainty on the estimation of $[W_s]$, which is defined in the same fashion as Equations 44 and 45. The maximum torque $\bar{\tau}_{max}$ is an estimate of the maximum value of the external torque $\bar{\tau}_{ext}$. Using Equation 49, the bound on F_2 can now be placed as

$$F_{2,UB} = [\hat{J}]^{-1}(D_J + I)[\dot{J}]_{max}\bar{\omega} \quad (54)$$

Where $[\dot{J}]_{max}$ is an estimate on the maximum value of the rate of change of the spacecraft moment of inertia $[\dot{J}]$. Thus, the uncertainty on the nominal dynamics can be described by

$$F = F_{1,UB} + F_{2,UB} \quad (55)$$

Similarly, the bounds on D_g [36] are shown to be given by

$$D_g = [\hat{J}]^{-1}(D_I + D_w + D_I D_w)[\hat{J}] \quad (56)$$

The reaction wheel uncertainties D_s and D_w are both assumed to a described by a maximum torque uncertainty d_r and alignment error from their nominal axis θ_r. The peak uncertainty matrices are modeled as [34]

$$D_s = D_w = \begin{bmatrix} d_r & (1+d_r)\theta_r & (1+d_r)\theta_r \\ (1+d_r)\theta_r & d_r & (1+d_r)\theta_r \\ (1+d_r)\theta_r & (1+d_r)\theta_r & d_r \end{bmatrix} \quad (57)$$

Additionally, the reaction wheel inertia uncertainty on each axis is assumed to be bounded by an uncertainty

$$J_{s_i} = (1 - \Delta_{J_s})\hat{J}_{s_i} \quad (58)$$

where $\mathrm{abs}(\Delta_{J_s}) \leq D_{J_s}$. The parameters d_r, θ_r, and D_{J_s} will have to be determined through hardware testing. In the current work, we place conservative estimates on these parameters to estimate the peak uncertainty of the spin alignment matrix. The peak inertia uncertainty bound D_J is estimated by concentrating the entire regolith mass at different locations inside the simulated regolith chamber and calculating the inertia tensor using Equation 13. This allows us to estimate the minimum and maximum elements of the inertia matrix. Let $[J_{min}]$, and $[J_{max}]$ denote matrices that contain maximum and minimum elements of the moment of inertia matrix respectively. Then from Equation 47, we can express the minimum and maximum values of the inertia matrix as

$$[J_{min}] = (I - \mathrm{D}_J)[\hat{J}]$$
$$[J_{max}] = (I + \mathrm{D}_J)[\hat{J}] \quad (59)$$

Which allows us to derive an expression for the peak moment of inertia uncertainty as

$$\mathrm{D}_J = \frac{1}{2}([J_{max}] - [J_{max}])[\hat{J}]^{-1} \quad (60)$$

The peak fluctuation rate $[\dot{J}]_{max}$ is estimated by placing conservative estimate such the transition from $[\dot{J}]_{max}$ *to* $[\dot{J}]_{min}$ occurs in one timestep Δt.

C. *Uncertainty Models*

In order to simulate the performance of the control law, we propagate the spacecraft attitude dynamics forward in time. The true dynamics will be propagated by modeling the parametric uncertainties of spacecraft parameters, specifically the inertia matrix, inertia fluctuation rate, reaction wheel alignment and reaction wheel inertia uncertainty, while the controller will be designed using the nominal estimates of these parameters.

Inertia Uncertainties. The fluctuation of true spacecraft moment of inertia is modeled by propagating the regolith motion forward in time and computing the moment of inertia, as described in Section IV, at every simulation timestep. The rate of change of inertia at simulation instant t is computed as

$$[\dot{J}](t) = \frac{[J](t) - [J](t - \Delta t)}{\Delta t} \quad (61)$$

Where Δt denotes the length of the simulation timestep. The nominal value of the inertia tensor is noted by concentrating the entire regolith at the center of the regolith chamber. As presented above, we assume that the inertia matrix of the nominal model does not fluctuate.

Reaction Wheel Uncertainties. In the case of AOSAT+, the reaction wheels will be placed along the three body frame axes presented in Fig. 4. Therefore, the nominal spin alignment matrix $[\hat{W}_s]$ is the 3×3 identity matrix I. The true alignment matrix $[W_s]$ is computed by rotating the nominal spin axes [34] as

$$[W_s] = \left[Y(\theta_1)Z(\theta_2)\hat{w}_{s_1} \quad X(\theta_3)Z(\theta_4)\hat{w}_{s_2} \quad X(\theta_5)Y(\theta_6)\hat{w}_{s_3}\right] \quad (62)$$

Where X, Y, and Z are principal rotation matrices about x, y, and z axes respectively [20]. The rotation angles θ_i are randomly created from a uniform distribution in $[-\theta_r, \theta_r]$. Additionally, since the attitude control system has three identical reaction wheels along its spin axes, we assume all reaction wheels have the same nominal spin axis moment of

inertia $\hat{J}_{s_i}$ which is estimated from the reaction wheel datasheet, while their true values are created from a uniform random distribution in $\left[\left(1-D_{J_s}\right)\hat{J}_{s_i},\ \left(1+D_{J_s}\right)\hat{J}_{s_i}\right]$.

D. Disturbance Torques

The spacecraft is subjected to orbital disturbance torques from the solar radiation pressure, atmospheric drag, and gravity gradient [17, 23]. Since these values vary based on the orbital location of the spacecraft, the orbit of the spacecraft is also propagated along with the regolith motion, and spacecraft attitude dynamics. The orbit is propagated using Cowell's method [40] with the nominal orbital elements presented in Table 2. The drag perturbation is modeled using the patched exponential atmospheric model [41]. The effect of solar radiation pressure is modeled using the cannonball model [42].

E. Actuator Constraints

The values computed by the control law in Equation 42 can be virtually unbounded. However, these cannot be always realized due to hardware limitations. Specifically, the reaction wheels are bounded by their peak control torque U_{max}, and peak spin rate Ω_{max}.

Torque Saturation. The peak control torque along a spin axis is capped at U_{max} whenever its magnitude of the commanded control torque component exceeds this value, i.e., its components are bounded by

$$U_i = \text{sign}(U_i)U_{max} \quad \text{if } \text{abs}(U_i) > U_{max} \tag{63}$$

Wheel Spin rate Saturation. The evolution of the reaction wheel spin rate along a spin axis is capped at Ω_{max} when the magnitude of spin along that axis exceeds Ω_{max}. Since the spin rates of the reaction wheels are the cause of their control torques, the commanded control torque along that axis is set to zero, i.e.

$$\Omega_i = \text{sign}(\Omega_i)\Omega_{max} \quad \text{if } \text{abs}(\Omega_i) > \Omega_{max}$$

and

$$U_i = 0 \quad \text{if } \text{abs}(\Omega_i) > \Omega_{max} \tag{64}$$

It should be noted here that the MRPs and reaction wheel spin rates updates described in Equations 20 and 64 are event-based state updates. Additionally, the computation of the inertia fluctuation using Equation 61 can become unstable when the timestep Δt approaches zero. For this reason, a fixed step, custom made fourth-order Runge-Kutta integrator [43] was implemented to propagate the spacecraft motion forward in simulation time.

Reaction Wheel Capacity. Due to their momentum exchange nature, the reaction wheels can only allow the spacecraft to have a controlled spin up to a certain magnitude, which is defined by the maximum reaction wheel spin rate. At a steady-state, the angular momentum exchange between a spacecraft and its reaction wheel aligned about the spin axis i is captured by the relation [24]

$$(J_i + J_{s_i})\omega_i = J_{s_i}\Omega_i \tag{65}$$

Where J_i is the principal moment of inertia element about the axis i, and J_{s_i} is the moment of inertia of the reaction wheel about its spin axis i. Equation 65 allows us to estimate the reaction wheel spin rate Ω_i required to spin the spacecraft with an angular velocity ω_i about the spin axis i.

F. Reference Attitude

As described in the previous section, the Centrifuge mode of the AOSAT+ mission will require the spacecraft body frame to spin over the orbital frame about its x-axis. The reference angular velocity is therefore given by

$$\bar{\omega}_{Ref} = \omega_{Ref}\begin{bmatrix}1\\0\\0\end{bmatrix} \tag{66}$$

Additionally, the spin axis during the Centrifuge mode should also be ensured to be aligned with the orbital x-axis as illustrated in Fig. 6. For this reason, a time-varying MRP profile is prescribed based on its principal angle-principal axis [20] definition as

$$\bar{\boldsymbol{\sigma}}_{\boldsymbol{Ref}} = \tan\left(\frac{\theta_{Ref}}{4}\right)\begin{bmatrix}1\\0\\0\end{bmatrix} \tag{67}$$

where the principal angle θ_{Ref} is calculated using

$$\theta_{Ref} = \text{mod}(\omega_{Ref}t|\ 2\pi) \tag{68}$$

The values for the reference spin magnitude ω_{Ref} are presented in Table 3. The modulo function in Equation 68 ensures that the principal angle is always bounded between $[0, 2\pi]$. Additionally, the reference MRP $\bar{\boldsymbol{\sigma}}_{\boldsymbol{Ref}}$ is switched to its shadow set using Equation 20 when its magnitude exceeds unity. Also, Equation 68 assumes that the spacecraft is at rest with its initial principal angle prior to entering the Centrifuge mode as zero.

VI. Numerical Simulations

This section simulates the performance of the AOSAT+ Centrifuge mode by implementing the sliding mode control law discussed above. We begin by estimating the bounds on the inertia related uncertainties due to regolith fluctuation, and initialization of regolith particles for the simulations. Following this, we proceed to the simulating the performance of the Centrifuge mode by implementing the sliding mode controller discussed in the previous section. Finally, we discuss the effectiveness of the control law and the attitude control actuators in realizing the Centrifuge mode of AOSAT+.

A. Inertia Uncertainty Estimates.

As described above, the bounds on spacecraft moments of inertia were estimated by concentrating the entire regolith mass of 2.5 kg at different corners, edge centers, and face centers of the simulated payload chamber. The total spacecraft moment of

inertia was then estimated using Equation 13 at each of these points. This scheme allowed us to sample about 27 boundary points on this payload chamber and estimate the maximum and minimum values of the elements inside the moment of inertia matrix of the spacecraft. The nominal moment of inertia is estimated by concentrating the regolith mass at the sample point located at the center of the simulated payload chamber. This is indicative of the case that the regolith is evenly distributed around the laboratory chamber of the spacecraft. The peak inertia uncertainty was then estimated using Equation 60. The different sample points used are presented in Fig. 14. The variation of elements of the net spacecraft moment of inertia tensor $[J]$ when regolith is concentrated at different sampling points in Fig. 14 are presented in Fig 15. The matrices describing the maximum and minimum values of the moment of inertia matrix, along with the nominal moment of inertia matrix are presented in Table 5. The peak inertia fluctuation rate was estimated by placing a conservative assumption that the shift from the $[J_{max}]$ to $[J_{min}]$ occurred within one simulation timestep Δt. The value of simulation was varied based on the number of particles being simulated in order to improve the computational performance of the simulations.

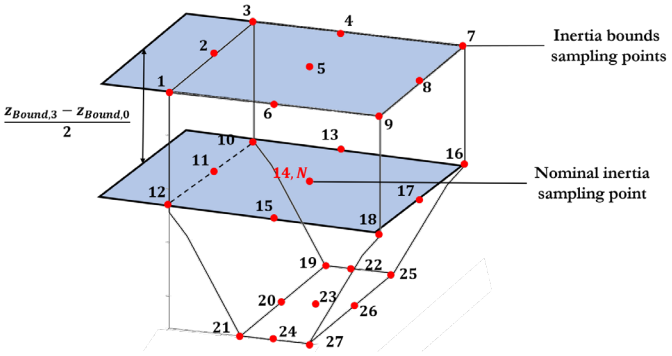

Fig. 14. The regolith concentration sample points used to estimate the peak inertia uncertainty and nominal spacecraft inertia matrix.

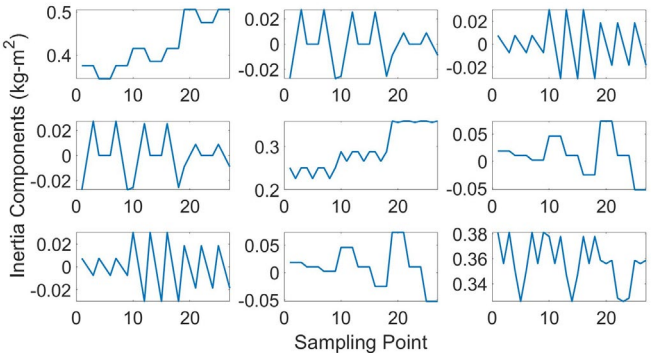

Fig. 15. Variation of the elements of the spacecraft inertia matrix due to concentrating regolith masses at different sampling points.

B. *Simulation Initialization*

We simulate the Centrifuge mode for three different regolith pools each having a different number of particles: i. $N = 100$, ii. $N = 1000$, and iii. $N = 10000$ particles.

Regolith Initialization. All simulations regolith particles were created with uniformly distributed masses, which were normalized such that their net mass remained a constant value of 2.5 kg which is the estimated mass of the net regolith onboard the AOSAT+ spacecraft. Each particle was assigned a radius which was a randomly distributed value between $1\ \mu$m to 1 cm, similar to the test pools simulated in Schwartz et al [37]. Studies have shown the coefficient of restitution, C_r of the type of regolith on AOSAT+ vary between 0.8 to 0.95 [44]. For this reason, each collision was assigned a random C_r which is uniformly distributed in the range $[0.8, 0.95]$. All particles were initialized at random locations inside the regolith chamber with their cartesian components uniformly distributed between their corresponding boundary values. The velocities of particles inside the spacecraft body frame were initialized with uniformly distributed random components in $[-1, 1]$ cm/s. A time step of $\Delta t = 0.2$ sec was used to simulate the case with $N = 100$ and $N = 1000$ particles, while a larger time step of $\Delta t = 1$ sec was used to simulate the case of $N = 10000$ particles. These timesteps were mainly selected to improve the computational performance of the simulations. Each spacecraft simulation ran for a total simulation timespan of 10 mins. The three different regolith pools used in the current study are visualized in Fig. 16.

Table 5. The nominal and extreme values of the spacecraft moment of inertia matrix.

Parameter	Value
Nominal spacecraft moment of inertia $[\hat{J}]$, (kg m^2)	$\begin{bmatrix} 0.385 & 0 & 0 \\ 0 & 0.266 & 0.01 \\ 0 & 0.01 & 0.326 \end{bmatrix}$
Maximum elements of the moment of inertia $[J_{max}]$ (kg m^2)	$\begin{bmatrix} 0.505 & 0.027 & 0.03 \\ 0.027 & 0.359 & -0.052 \\ 0.03 & -0.052 & 0.381 \end{bmatrix}$
Minimum elements of the moment of inertia $[J_{min}]$ (kg m^2)	$\begin{bmatrix} 0.345 & -0.027 & -0.03 \\ -0.027 & 0.226 & 0.01 \\ -0.03 & 0.01 & 0.326 \end{bmatrix}$

Spacecraft Initialization. The reference attitude of the spacecraft (Equations 66 and 67) during the Centrifuge mode is described assuming the spacecraft is initially at rest with its orbit and body frames initially aligned. Therefore, we initialize the attitude of the spacecraft with its MRP components following a uniform random distribution in the range $[-0.01, 0.01]$. The angular velocity components of the spacecraft are initialized as uniformly distributed random numbers between $[-0.001, 0.001]$ RPM, while the reaction wheels are initialized with random initial spin rates $[-10, 10]$ RPM. The performance of the Centrifuge mode with each of the three regolith pools is run multiple times for each reference spin rate ω_{Ref}, with random attitude and regolith initializations and parametric uncertainties. The parameters corresponding to the simulated RWp050 reaction wheels of the BCT XACT 50 ADCS module, used in estimating their peak

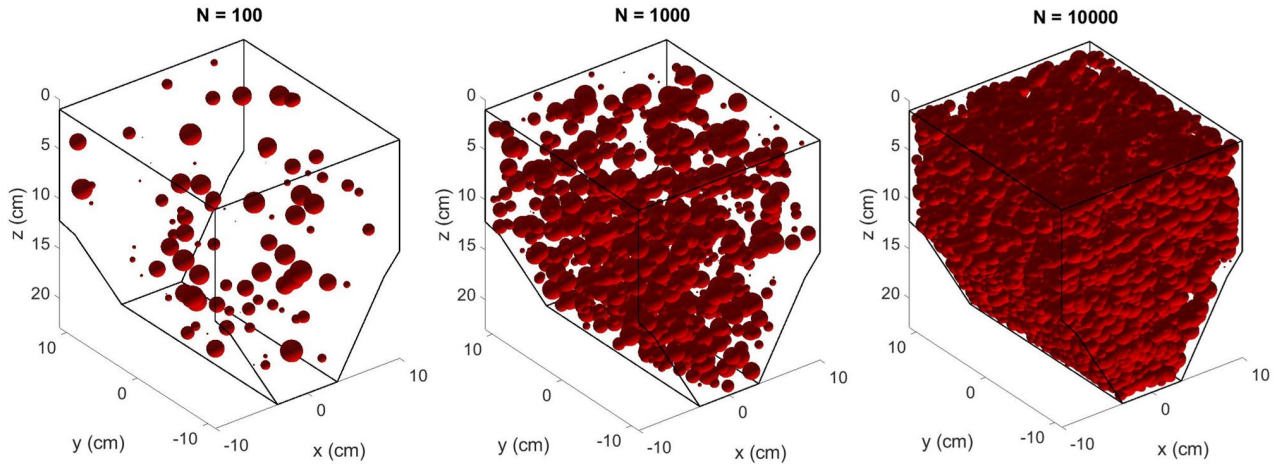

Fig. 16. The three regolith pools that are used in the current work to study the Centrifuge mode.

and nominal uncertainties are presented in Table 6. The uncertainty parameters in Table 6 are based on conservative estimates, while the nominal value is estimated based on the specifications of the selected hardware.

As mentioned above, the orbit of the spacecraft was also propagated in order to simulate the orbital disturbance torques such as drag, SRP, and gravity gradient torques. The fixed orbital elements of the spacecraft during the initialization are noted from Table 2. The true anomaly during the initialization is a uniformly distributed random number between $[0, 2\pi]$. A drag coefficient of 2.2 is assumed since the spacecraft surfaces are mainly rectangular [44]. The Solar direction, for estimating the SRP disturbance, is determined by computing the ephemeris of Earth based on a Julian date [35] which is randomly sampled during the timespan $2025 - 2026$. A peak effective cross-sectional area of 3546 $\text{cm}^2$is used as the reference area for estimating the drag and solar radiation pressure, as this is an estimate of the maximum surface area exposed when the spacecraft is in the deployed configuration.

Table 6. Uncertainty modeling parameters used in the current work.

Parameter	Value
Maximum torque fraction uncertainty d_r (%)	10
Maximum alignment error θ_r (deg)	1
Maximum wheel inertia uncertainty Δ_{J_s} (%)	10
Nominal wheel inertia Δ_{J_s} (kg m^2)	1.01×10^{-4}

The gains of the sliding mode controller were tuned based on a trial and error method, were a smooth tracking was consistently observed. The selected gains of the sliding mode control law are presented in Table 7.

Table 7. The selected gain parameters used in implementing the sliding mode control law.

Parameter	Value
K_P (rad/s)	$0.14\, I$
K_I (rad/s^2)	$5.4 \times 10^{-4} I$
η (rad/s^2)	$[0.01 \quad 0.5 \quad 0.5]^T$
Φ (rad/s)	$[1 \quad 1 \quad 1]^T$
$\bar{\tau}_{max}$ ($\text{N} - \text{m}$)	$10^{-5}[1 \quad 1 \quad 1]^T$

C. *Centrifuge Mode Simulations*

The results of the Centrifuge mode simulations for different test cases are presented here. We begin by noting the peak disturbances, spacecraft attitudes, and centrifugal accelerations generated at the bottom of the simulated laboratory chamber are noted here.

Case $N = 100$: The spacecraft was initialized with 10 random initial conditions per reference spin rate magnitude as described above. The attitude of the spacecraft was controlled using the sliding mode controller with gains in Table 7. The effect of regolith fluctuation torque ($[J]^{-1}[\dot{J}]\bar{\omega}$), along with the other disturbance torques modeled in the current work, are presented in the semilog plot in Fig. 17. As seen here, the inertia fluctuation presents the dominant source of disturbance torques, on the order of 10^{-4} $\text{N} - \text{m}$ in the first two studies which have lower target spin rate magnitudes. The maximum inertia fluctuation torque occurred around of 10^{-3} $\text{N} - \text{m}$ when the target spin rate was a maximum of 1.1 RPM. The inertia fluctuation torques are followed by the gravity gradient (around $10^{-8} - 10^{-7}$ $\text{N} - \text{m}$), SRP (around 10^{-7} $\text{N} - \text{m}$), and the drag torques (around 10^{-10} $\text{N} - \text{m}$).

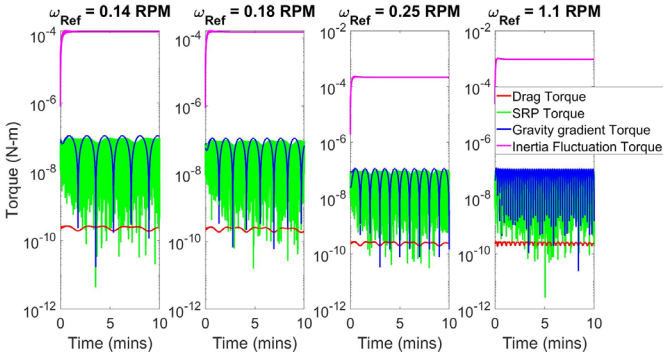

Fig. 17. Disturbance torques acting on the simulated Centrifuge mode at different target spin rates, when the chamber has $N = 100$ particles.

The response of the spacecraft angular velocity components, and the MRP components are presented in Figs. 18 and 19 respectively. As seen in Fig 18, the simulations indicate that the spacecraft is able to steadily achieve the desired spin rates within 1.5 mins. Fig. 19 suggests that the spacecraft is able to track its reference MRP, which indicates that the spin axis is kept aligned with the orbital x-axis.

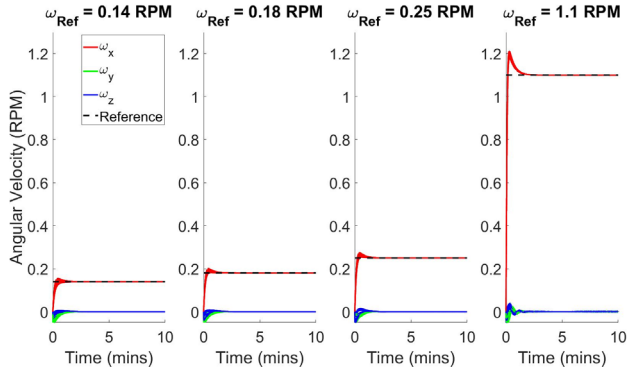

Fig. 18. Spacecraft angular velocity response for different target spin rates of the Centrifuge mode, when the chamber has $N = 100$ particles.

The centrifugal accelerations generated at the bottom of the AOSAT+ laboratory chamber, computed using Equation 14, are presented in Fig. 20. As seen here, the magnitude of centrifugal acceleration at the bottom of the laboratory chamber is able to meet the gravity levels of their target small bodies.

Case $N = 1000$: The disturbance torques modeled on the spacecraft are presented in Fig. 21. As seen here, the inertia fluctuation torque is largely on the same order of magnitude (around 10^{-7} N − m) as the gravity gradient and the SRP torques at slower rotation speeds. The magnitude is seen to steadily go up to 10^{-6} N − m at the maximum target spin rate of 1.1 RPM.

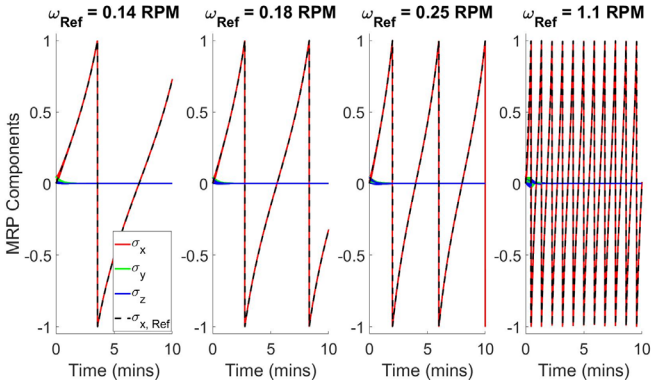

Fig. 19. Time response of the spacecraft MRP components at different target spin rates of the Centrifuge mode, when $N = 100$ particles.

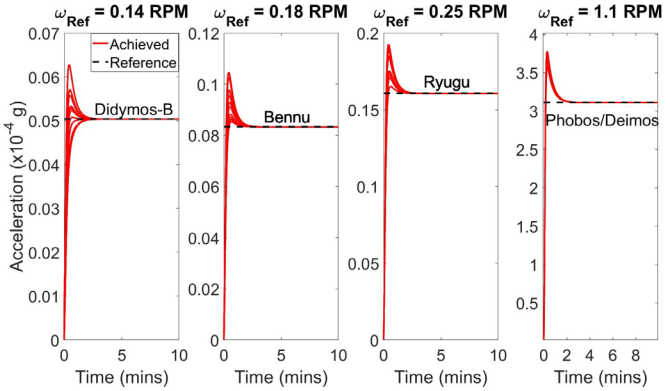

Fig. 20. Magnitude of centrifugal accelerations generated at the bottom of the AOSAT+ laboratory chamber when $N = 100$ particles.

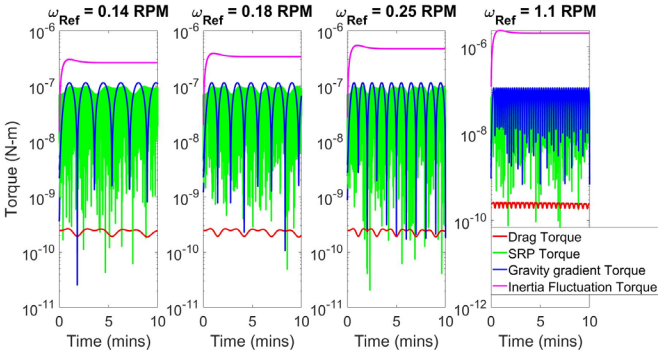

Fig. 21. Disturbance torques acting on the simulated Centrifuge mode at different target spin rates, when the chamber has $N = 1000$ particles.

The response of the spacecraft angular velocity components is presented in Fig. 22. As seen here the spacecraft is able to track the desired target spin rates about the orbital x-axis within 3 minutes. The time evolution of the MRP components of the spacecraft (not shown here) is noted to follow the same reference trajectory noted in Fig. 19.

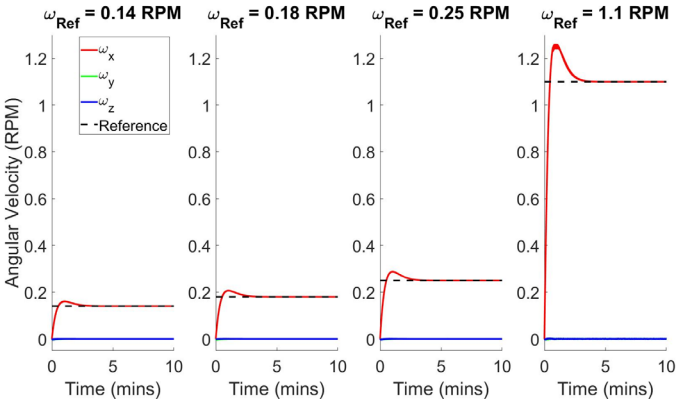

Fig. 22. Spacecraft angular velocity response for different target spin rates of the Centrifuge mode, when the chamber has $N = 1000$ particles.

The centrifugal accelerations generated at the bottom of the AOSAT+ laboratory chamber, are presented in Fig. 23. As seen here, the magnitude of centrifugal acceleration at the bottom of the laboratory chamber is able to achieve the gravity levels of their target small bodies.

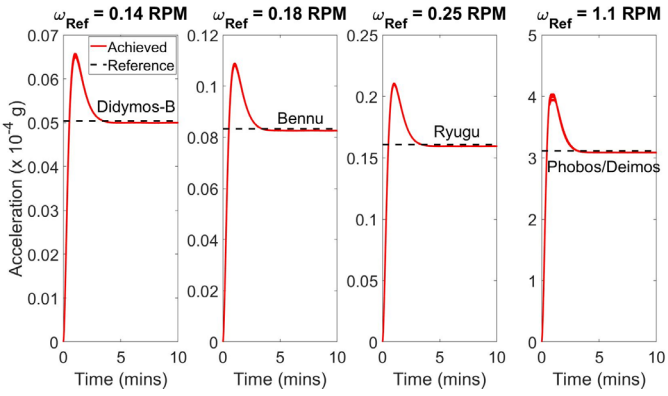

Fig. 23. Centrifugal accelerations generated at the bottom of the AOSAT+ laboratory chamber when $N = 1000$ particles.

Case $N = 10000$: In the case of $N = 10000$ particles, two simulations per reference spin rate were carried out, due to its intense computational load. The disturbance torques modeled on the spacecraft are presented in Fig. 24. As seen here, the inertia fluctuation has a magnitude around 10^{-7} N − m, when the commanded spin rate, was 0.14 RPM, which then rises to around 10^{-6} N − m for a target spin 1.1 RPM. At the slowest target spin rate, the gravity gradient forms the dominant source of perturbation torques followed by the SRP and the drag torques. The inertia fluctuation gradually increases with the increasing spin rate due to its proportional relation to the spacecraft angular velocity. Comparing Fig. 17, 21, and 24, it can be seen that the magnitude of the perturbation caused by the inertia fluctuation is shown to decrease. This seems to agree with the intuitive reasoning that as the number of particles in the simulated pool increases, the average mass of particles in the pool decreases (since total mass is constant), which reduces their inertia contribution of each particle to the spacecraft. Additionally, the maximum range of the inertia fluctuation torques noted in the current work appeared to range from 10^{-6} to 10^{-4} N − m, which was mainly noted during the maximum target spin rate of 1.1 RPM. The case corresponding to 10^{-4} N − m was when the simulated regolith pool had $N = 100$ particles. The real mission will carry around $N = 10000$ to $N = 100000$ particles. Therefore, we estimate a peak disturbance torque of up to 10^{-6} N − m due to the regolith fluctuations based on the current work. However, it is made explicit here that due to the assumptions such as hard sphere collisions, and timestep constraints, the accuracy of this peak inertia fluctuation torque magnitude needs to be experimentally verified in future work.

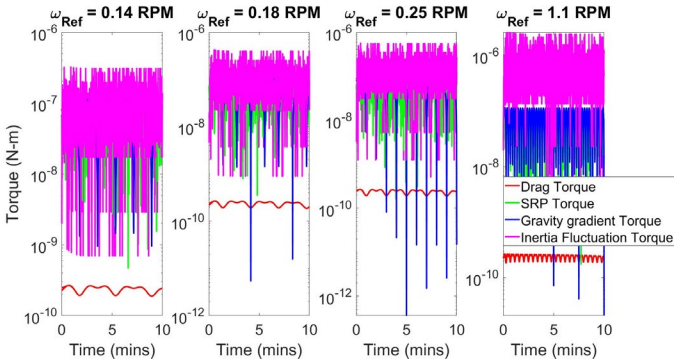

Fig. 24. Disturbance torques acting on the simulated Centrifuge mode at different target spin rates, when the chamber has $N = 10000$ particles.

The response of the spacecraft angular velocity components is presented in Fig 25. As seen here the simulations indicate that the spacecraft is able to converge steadily with all four desired spin rates within 1.5 mins.

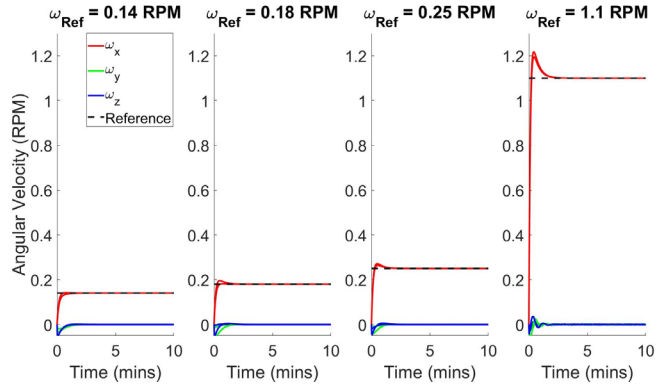

Fig. 25. Spacecraft angular velocity response for different target spin rates of the Centrifuge mode, when the chamber has $N = 10000$ particles.

The centrifugal accelerations generated at the bottom of the AOSAT+ laboratory chamber, are presented in Fig. 26. As seen here, the magnitude of centrifugal acceleration at the bottom of the laboratory chamber is able to meet the gravity levels of their target small bodies.

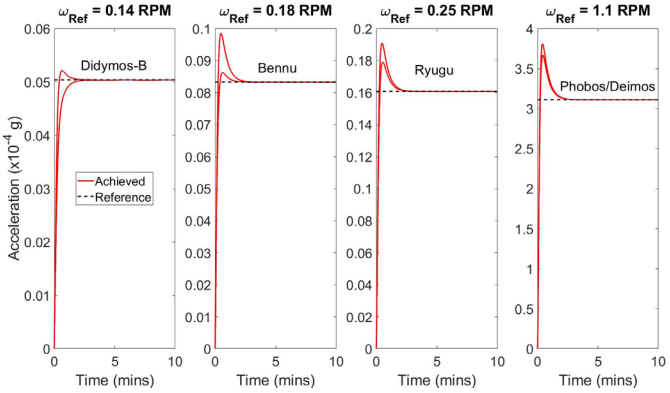

Fig. 26. Centrifugal accelerations generated at the bottom of the AOSAT+ laboratory chamber when $N = 10000$ particles.

D. Control Law Performance

The performance of the sliding mode control law is examined in this section. As a baseline case, we examine the operation of the control law for the case of $N = 1000$ particles. The commanded control torques executed by the simulated reaction wheels are presented in Fig. 27. As seen here, the peak control torque noted during the simulation is about $2.5\ \text{mN} - \text{m}$ which was computed during the maximum target spin rate of 1.1 RPM. The peak torque supplied by the XACT-50 reaction wheels is $7\ \text{mN} - \text{m}$. This suggests that the Centrifuge mode can be executed by using about 35.7% of the peak actuator control torque.

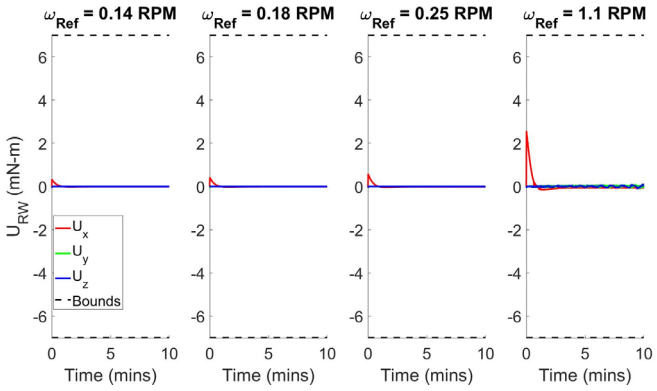

Fig. 27. Reaction wheel control torque history for different target spin rates.

The evolution of the sliding surface variable S is presented in Fig 28. The history of the surface variable is noted using Equation 34. The integral term in Equation 34 was computed as the cumulative sum of the error MRP computed using Equation 36. But the error MRP, and the cumulative error sum were regulated by switching to their shadow sets, when necessary, using Equation 20. As seen here, the cartesian components of S are shown to converge steadily to a maximum of $0.004\ \text{rad/sec}$ noted during the target spin rate of 1.1 RPM. As noted in Fig. 27, the x-component of the sliding variable is the dominant contribution to the error, which is caused mainly to the latency in moving from the current attitude state of the spacecraft to its commanded reference.

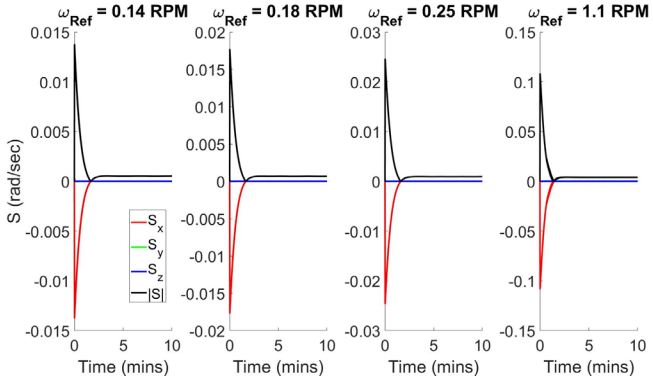

Fig. 28. Evolution of the sliding surface variable S noted for different target spin rates.

The nominal and robust components of the sliding mode control torque are presented in Fig 29 and 30 respectively. As seen here, the nominal torque in all cases, approaches to a steady value 0 along the x-axis, the off-axis are seen to slightly oscillate in order to steadily hold the spin axis.

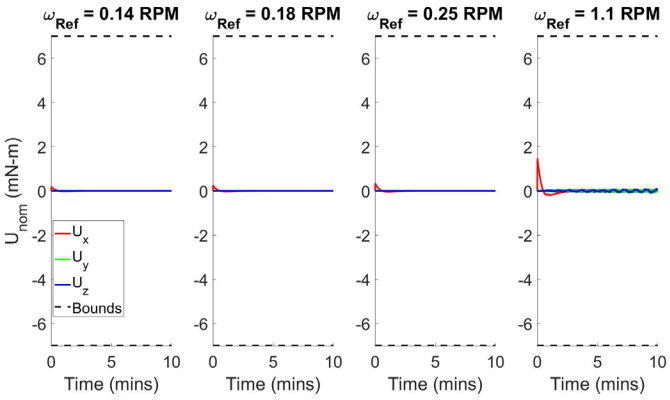

Fig. 29. Nominal control torque component-wise history generated by the sliding mode controller during different target spin rates.

The robust control gain history presented in Fig. 29 indicates that the controller converges to a steady-state value of $0.05\ \text{mN} - \text{m}$, in order to keep the evolution of attitude along the sliding surface S while satisfying the reachability condition described by Equation 44.

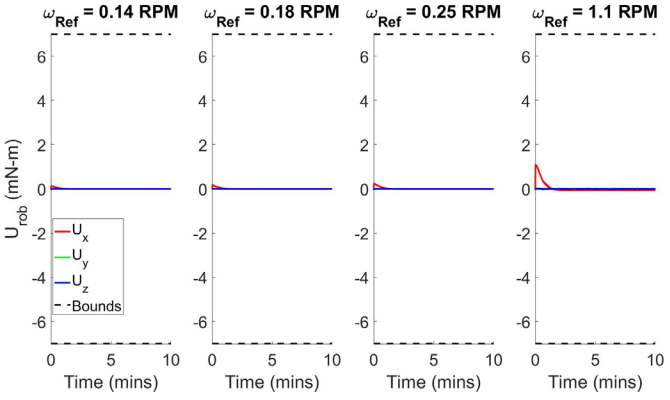

Fig. 30. Robust control torque component-wise history generated by the sliding mode controller during different target spin rates.

E. Actuator Performance

The performance of the reaction wheels during the baseline Centrifuge mode simulations ($N = 1000$ particles) is presented here. As shown above, the peak control torque to spin the spacecraft at 1.1 RPM was well within the bounds of the actuator. In addition, the reaction wheels are limited by their spin angular velocities. The time evolution of the reaction wheel spin rates is presented in Fig. 31. Here it is noted that the reaction wheels approach a steady-state, indicative of their momentum exchange operation, once the spacecraft target spin rate is achieved. As seen from Fig. 31, the reaction wheels stabilized to about 533 RPM in order to spin the spacecraft at a spin rate of 0.14 RPM. The target spin rate of 0.18 RPM required the reaction wheels to spin at 688 RPM, the spin rate of 0.25 RPM required around 955 RPM, and the maximum spin rate of 1.1 RPM was achieved by the wheels stabilizing at 4123 RPM. The maximum rated spin rate of the RWp050 reaction wheels is about 4731 RPM, which indicates that the reaction wheels are capable of achieving the target spin rates of the AOSAT+ mission.

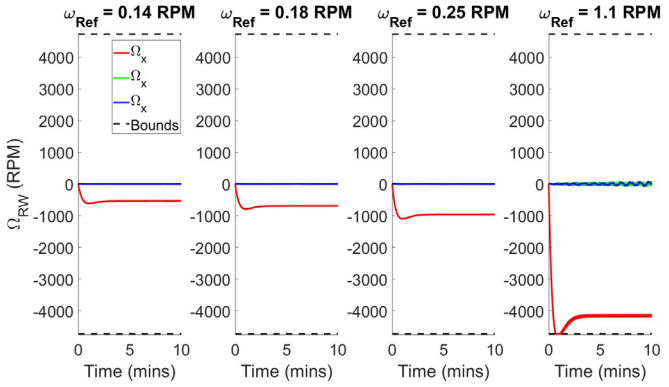

Fig. 31. Time evolution of the reaction wheel spin rates noted during different target spacecraft spin rate simulations.

While the reaction wheel spin rates in Fig. 30 indicated that the spin rates are within the maximum rated spin rates of the actuator the performance bounds still need to be established. This is carried out by noting the reaction wheel speeds required to induce the target centrifuging spin rates for the spacecraft using Equation 65. The relation between the spacecraft spin rates and reaction wheel spin rates is presented in Fig 32. The nominal, minimum, and maximum moments of inertia are noted in Table 5. The minimum, nominal, and maximum spin rates of the reaction wheels required to induce the target centrifuging spins are presented in Table 8. As noted from Table 8, the reaction wheel spin rate required to spin the spacecraft at 1.1 RPM was found to be about 5513 RPM when the spacecraft had the worst case moment of inertia about the spin axis, which is around 16 % larger than the maximum rated spin rate of the reaction wheels. However, the worst-case risk assumes the condition that the entire regolith is concentrated at one of the bottom face corners of the simulated regolith chamber as shown in Fig. 14, which is a strictly conservative assumption. On the off chance that the reaction wheels are saturated during the maximum spin maneuver of rotating at 1.1 RPM, the spacecraft will detumble and desaturate its reaction wheels using the magnetorquers.

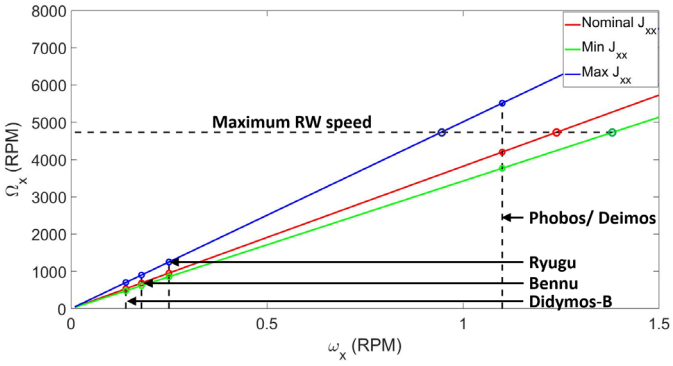

Fig. 32. Reaction wheel spin rates required to spin the spacecraft about its centrifuge axis.

Table 8. Variation of the required reaction wheel spin rate at with the targeted spacecraft spin rate.

Target spacecraft spin rate (RPM)	Required reaction wheel spin rate (RPM)		
	Min.	Nominal	Max.
0.14	479	535	702
0.18	616	678	902
0.25	856	955	1253
1.1	3767	4202	5513

Additionally, this also allows us to better design the laboratory chamber, in order to ensure that the worst-case regolith concentrations do not occur inside the laboratory. The maximum reaction wheel spin rate required to spin AOSAT+ at 1.1 RPM was about 4202 RPM which is around 89 % of the maximum rated reaction wheel spin rate for the case of nominal spacecraft inertia, which occurs when the regolith is uniformly distributed around the regolith chamber. This configuration is more likely because of the large number of regolith particles inside the original spacecraft chamber. Therefore, the RWp050 reaction wheels are still able to meet all the requirements of the AOSAT+ Centrifuge mode, for the nominal design of the spacecraft.

F. Discussion

The results of the simulation in the current work provide key insights into implementing the Centrifuge mode of the AOSAT+ mission. Firstly, for a constant net regolith mass, the disturbance torques decreased as the number of regolith particles in the simulated pool increased. As a baseline estimate, the disturbance torques arising from fluctuating regolith is noted to be around $10^{-6} - 10^{-7}$ mN − m, and can become the dominant source of perturbation torques at high-speed target rotations of around 0.25 to 1.1 RPM. Secondly, the designed sliding mode control torque is capable of rotating the spacecraft

at all its target rotation speeds in the presence of inertia fluctuations, parametric uncertainties, and orbital disturbances. Additionally, the control torques generated during the simulations were well within the boundaries of the selected BCT XACT-50 attitude determination and control system (ADCS) module, where simulations indicate that the spacecraft can converge to its target speeds within 3 mins by using about 36 % of the peak actuator torque. Finally, the simulations and an angular momentum exchange analysis suggest that the RWp050 reaction wheels of the XACT-50 module are capable of meeting all the requirements of the Centrifuge mode is the nominal case, where regolith is assumed to be evenly distributed about the center of the laboratory chamber. However, the current work also identifies that some worst-case distributions can saturate the reaction wheels when trying to spin the spacecraft its maximum target spin rate of 1.1 RPM. However, this allows us to better design the laboratory chamber of the spacecraft, in order to make ensure the successful operation of the AOSAT+ spacecraft.

The following are some of the key contributions of the current work to the existing state of the art in the field of small spacecraft technology. Firstly, the current work presented a novel CubeSat mission concept from an attitude control point of view. The AOSAT+ mission will aim to advance CubeSats as platforms to conduct planetary science research. Secondly, the current work identified some of the key attitude control challenges of operating a dedicated centrifuging spacecraft. In the current work, we developed a combined platform for modeling regolith fluctuations using an N-body discrete element model (DEM) of regolith, coupled with a spacecraft attitude dynamics simulator. In addition, modeling methods to model and conservatively bound the uncertainty due to fluctuations was also presented. Following this, we derived a sliding mode control law in order to robustly track a reference attitude during its Centrifuge mode. The controller was designed in order to handle the fluctuations in the spacecraft moment of inertia along with parametric uncertainties. Here, key design constraints on implementing the control law with realistic actuator constraints such as control torque and reaction wheel saturation were presented. Finally, the performance of the control law on the spacecraft Centrifuge was successfully demonstrated in the presence of the modeled fluctuations and uncertainties, allowing us to gain important insights into the operation of the Centrifuge mode,

VII. CONCLUSION

This work presented the goals and challenges of the AOSAT+ mission from an attitude control perspective. The AOSAT+ is a 12U CubeSat mission whose objective is to simulate the gravity of small bodies such as asteroids, by acting as a dedicated space-based centrifuge for 2.5 kg of crushed Allende meteor regolith. During this centrifuging maneuver, the spacecraft will be spun at different target spin rates about its body axis, which will then induce centrifugal acceleration components that correspond to gravity levels of a target asteroid at the maximum radial moment arm. We began by presenting a detailed description of the AOSAT+ spacecraft, and its subsystems. The different planned modes of spacecraft operation were also presented. While most of these planned operations are typical of any spacecraft mission with three axis-attitude control, the Centrifuge mode of AOSAT+ mission is a unique mission operation as it requires the spacecraft to be spinning about a fixed axis during its orbit. Additionally, the Centrifuge mode will also contain moving regolith particles which will cause the moment of inertia to fluctuate during the mission. In order to address this, we derived a robust control law that can handle the inertia fluctuations and other parametric uncertainties. The perturbation due to inertia fluctuation was modeled using an N-body DEM based model of regolith which treated regolith particles as inelastically colliding hard spheres. A detailed discussion on implementing the designed control law on the selected off-the-shelf ADCS actuators was provided. Finally, the control law was successfully demonstrated at all the target spin rates for the nominal spacecraft design, and the control laws and actuator performance were thoroughly analyzed, which allowed us to identify key insights and important design considerations on realizing the Centrifuge mode on the AOSAT+ spacecraft.

While the current work presented a unified simulation scheme for simulating the regolith motion and the spacecraft attitude motion, some assumptions were made on the regolith grains such as the nature of collisions and the shape of the particles in order to improve computational performance. Future work on AOSAT+ will try to address these issues by modeling the regolith motion using non-uniform grains along with soft collisions. This will help us improve the accuracy of the disturbance torques on AOSAT+ which were identified by the current work. In addition, future work will focus on validating the control algorithms developed in the current work through hardware in loop testing of the AOSAT+ spacecraft subsystems. If successfully realized, this will enable AOSAT+ to simulate and study the surface of asteroids inside a low Earth orbiting CubeSat, which will advance the legacy of small spacecraft as platforms to conduct planetary science research and provide new pathways and tools to explore our solar system.

REFERENCES

[1] D.S. Lauretta, S.S. Balram-Knutson, E. Beshore, W. Boynton, C.D. d'Aubigny, D.N. DellaGiustina, H.L. Enos, D.R. Golish, C.W. Hergenrother, E.S. Howell and CA Bennett, 2017. OSIRIS-REx: sample return from asteroid (101955) Bennu. *Space Science Reviews*, *212*(1-2), pp.925-984.

[2] Y. Tsuda, M. Yoshikawa, M. Abe, H. Minamino. and S. Nakazawa, S., 2013. System design of the Hayabusa 2—Asteroid sample return mission to 1999 JU3. *Acta Astronautica*, *91*, pp.356-362.

[3] P.E. Michel et al., 2015. *Asteroids IV*, University of Arizona Press.

[4] J.C. Castillo-Rogez, M. Pavone, J.A. Hoffman, and I.A. Nesnas, 2012, March. Expected science return of spatially extended in-situ exploration at small solar system bodies. In *2012 IEEE Aerospace Conference* (pp. 1-15). IEEE.

[5] Thangavelautham, J., Asphaug, E. and Schwartz, S., 2019, March. An On-Orbit CubeSat Centrifuge for Asteroid Science and Exploration. In *2019 IEEE Aerospace Conference*. IEEE

[6] R.C. Griffith, 2011. *Mobile CubeSat command and control (MC3)*. Naval Postgraduate School, Monterey Ca.

[7] L.M. Sharp, 2011. *Three-dimensional critical wetting experiment in commercial zero-gravity space flight* (Doctoral dissertation, Purdue University).

[8] J.C. Jairala, R. Durkin, R.J. Marak, S.A. Sipila, Z.A. Ney, S.E. Parazynski, and A.H. Thomason, 2012. EVA Development and Verification Testing at NASA's Neutral Buoyancy Laboratory.

[9] W.A. Dittrich, 2014. Drop Tower Physics. *The Physics Teacher*, *52*(7), pp.415-417.

[10] L.R. Young, 2011, March. Spinning our way to Mars. In *Proceedings of the 2011 IEEE Aerospace Conference* (pp. 1-2). IEEE Computer Society.

[11] A.L. Paul and R.J. Ferl, 2015. Spaceflight exploration in plant gravitational biology. In *Plant Gravitropism* (pp. 285-305). Humana Press, New York, NY.

[12] G.H. Kitmacher, 2006. *Reference guide to the international space station*.

[13] Nason, I., Puig-Suari, J. and Twiggs, R., 2002, March. Development of a family of picosatellite deployers based on the CubeSat standard. In *Proceedings, IEEE Aerospace Conference* (Vol. 1, pp. 1-1). IEEE.

[14] J. Lightholder, A. Thoesen, E. Adamson, J. Jakubowski, R. Nallapu, S. Smallwood, L. Raura, A. Klesh, E. Asphaug, and J. Thangavelautham, 2017. Asteroid origins satellite (AOSAT) I: an on-orbit centrifuge science laboratory. *Acta Astronautica*, *133*, pp.81-94.

[15] Asphaug, E. and Thangavelautham, J., 2014, March. Asteroid regolith mechanics and primary accretion experiments in a CubeSat. In *45th Lunar and Planetary Science Conference* (p. 2306).

[16] Asphaug, E., Thangavelautham, J., Klesh, A., Chandra, A., Nallapu, R., Raura, L., Herreras-Martinez, M. and Schwartz, S., 2017. A CubeSat centrifuge for long duration milligravity research. *npj Microgravity*, *3*(1), pp.1-5.

[17] R. Nallapu, S. Shah, E. Asphaug, J. Thangavelautham*, Attitude control of the Asteroid Origins Satellite 1 (AOSAT 1).* AAS GNC Conference 2017.

[18] Schwartz, S.R., Michel, P. and Richardson, D.C., 2013. Numerically simulating impact disruptions of cohesive glass bead agglomerates using the soft-sphere discrete element method. *Icarus*, *226*(1), pp.67-76.

[19] Richardson, D.C., Quinn, T., Stadel, J. and Lake, G., 2000. Direct large-scale N-body simulations of planetesimal dynamics. *Icarus*, *143*(1), pp.45-59.

[20] Baraff, D., 1997. An introduction to physically based modeling: rigid body simulation II—nonpenetration constraints. *SIGGRAPH course notes*, pp. D31-D68.

[21] Murdoch, N., Sánchez, P., Schwartz, S.R. and Miyamoto, H., 2015. Asteroid Surface Geophysics. *Asteroids IV*, pp.767-792.

[22] Durda, D.D., Movshovitz, N., Richardson, D.C., Asphaug, E., Morgan, A., Rawlings, A.R. and Vest, C., 2011. Experimental determination of the coefficient of restitution for meter-scale granite spheres. *Icarus*, *211*(1), pp.849-855.

[23] F.L. Markley and J.L. Crassidis, 2014. *Fundamentals of spacecraft attitude determination and control* (Vol. 33). New York: Springer.

[24] J. Schaub, J. Junkins, 2014. *Analytical mechanics of space systems* 3rd ed., Reston, Va.: American Institute of Aeronautics and Astronautics.

[25] Terzakis, G., Lourakis, M. and Ait-Boudaoud, D., 2018. Modified Rodrigues Parameters: an efficient representation of orientation in 3D vision and graphics. *Journal of Mathematical Imaging and Vision*, *60*(3), pp.422-442.

[26] Roberson, R.E., 1979. Two decades of spacecraft attitude control. *Journal of Guidance and Control*, *2*(1), pp.3-8.

[27] Janssens, F.L. and van der Ha, J.C., 2011. On the stability of spinning satellites. *Acta Astronautica*, *68*(7-8), pp.778-789.

[28] Ibrahim, R.A., 2005. *Liquid sloshing dynamics: theory and applications*. Cambridge University Press.

[29] Souza, A.G., 2013. Study of the effects of liquid movement and flexibility in performance and robustness of the attitude control system of an artificial satellite [Master of Space Mechanics and Control]. *National Institute for Space Research (INPE), Sao José dos Campos, Brazil*.

[30] Zhengfeng, B. and Yang, Z., 2012. Attitude motion of spacecraft during oblique solar panel deployment. *Aircraft Engineering and Aerospace Technology*, *84*(2), pp.109-114.

[31] DeSouza, L.G., 1970. Robust controller design for a flexible space system using a combination of LQG/LTR and PRLQG methods. *WIT Transactions on The Built Environment*, *22*.

[32] DeSouza, L.G. and de Souza, A.G., 2014. Satellite attitude control system design considering the fuel slosh dynamics. *Shock and Vibration*, *2014*.

[33] Slotine, J.J.E. and Li, W., 1991. *Applied nonlinear control* (Vol. 199, No. 1). Englewood Cliffs, NJ: Prentice hall.

[34] Goeree, B.B. and Fasse, E.D., 2000, June. Sliding mode attitude control of a small satellite for ground tracking maneuvers. In *Proceedings of the 2000 American Control Conference. ACC (IEEE Cat. No. 00CH36334)* (Vol. 2, pp. 1134-1138). IEEE.

[35] Crassidis, J.L. and Markley, F.L., 1996. Sliding mode control using modified Rodrigues parameters. *Journal of Guidance, Control, and Dynamics*, *19*(6), pp.1381-1383.

[36] S. Kowalchuk and C. Hall, 2008, August. Spacecraft attitude sliding mode controller using reaction wheels. In *AIAA/AAS Astrodynamics Specialist Conference and Exhibit* (p. 6260).

[37] Schwartz, S.R., Thangavelautham, J., Asphaug, E., Chandra, A. and Vance, L., 2019. Investigating Asteroid Surface Geophysics with an Ultra-Low-Gravity Centrifuge in Low-Earth Orbit. Proceedings of the 70th International Astronautical Congress, IAF, Washington D.C.

[38] Stadel, J.G., 2001. *Cosmological N-body simulations and their analysis* (Doctoral dissertation, University of Washington).

[39] E.J. Lefferts, F.L. Markley, and M.D. Shuster, 1982. Kalman filtering for spacecraft attitude estimation. *Journal of Guidance, Control, and Dynamics*, *5*(5), pp.417-429.

[40] Vallado, D.A, 2013. Fundamentals of Astrodynamics and Applications, Fourth Edition, *Space Technology Library.*

[41] Guettler, D.B., 2007. *Satellite Attitude Control Using Atmospheric Drag* (No. AFIT/GA/ENY/07-M10). Air Force Inst Of Tech Wright-Patterson AFB OH Graduate School of Engineering and Management.

[42] J.W. McMahon, 2011. *An analytical theory for the perturbative effect of solar radiation pressure on natural and artificial satellites* (Doctoral dissertation, the University of Colorado at Boulder).

[43] Butcher, J.C., 1996. A history of Runge-Kutta methods. *Applied numerical mathematics*, *20*(3), pp.247-260.

[45] Wertz, J.R., Everett, D.F. and Puschell, J.J., 2011. *Space mission engineering: the new SMAD*. Microcosm Press.

BIOGRAPHY

Ravi Teja Nallapu *received a B.Tech. in Mechatronics Engineering from JNTU, Hyderabad, India in 2010. He then received an M.S in Aerospace Engineering from the University of Houston, TX in 2012. After this, he worked with U.S Airways as a Flight Simulator Engineer for 2 years. He is presently pursuing his Ph.D. in Aerospace Engineering from the University of Arizona, Az. He specializes in control theory and robotics. His research interests include GNC of spacecrafts, space systems engineering, orbital mechanics, and exploration robotics.*

Stephen R. Schwartz *graduated as a Bachelor of Arts from Columbia University with majors in Astronomy and Philosophy and obtained his Ph.D. in Astronomy/Astrophysics from The University of Maryland in College Park. His research focus includes studies into the ultra-low gravity mechanical environments of small asteroids, the effects of weak cohesion between the constitutive rubble that comprise these bodies, and what this can tell us about the formation histories of asteroids and comets and about the evolutionary history of our Solar System. After three years at the Department of Theoretical and Observational Planetology at the Observatoire de la Côte d'Azur in Nice, France, he is now at the University of Arizona's Lunar and Planetary Laboratory, which is well suited to his strong interests in space sciences and exploration. He currently serves on the science teams of two asteroid sample-return missions, as a Participating Scientist on NASA's OSIRIS-REx mission and as Co-Investigator on multiple instruments of JAXA's Hayabusa2 mission.*

Erik Asphaug *graduated in Mathematics and English from Rice University, taught high school for three years in Tucson, and obtained his Ph.D. in Planetary Sciences from the University of Arizona in 1993. After a postdoc at NASA Ames, he was hired and helped found the Planetary Sciences program at UC Santa Cruz. His signature research has been the geology of comets and asteroids, the physics of collisions, and planet formation. Since being at University of Arizona's Lunar and Planetary Laboratory he has been able to combine his deep interests, in theory, laboratory work, and space exploration, for example, as the Science PI of AOSAT I, a microgravity research centrifuge selected by NASA for launch, whose goal is to answer primary questions about accretion physics and asteroid regolith environments.*

Jekan Thangavelautham *has a background in aerospace engineering from the University of Toronto. He worked on Canadarm, Canadarm 2 and the DARPA Orbital Express missions at MDA Space Missions. Jekan obtained his Ph.D. in space robotics at the University of Toronto Institute for Aerospace Studies (UTIAS) and did his postdoctoral training at MIT's Field and Space Robotics Laboratory (FSRL). Jekan Thanga is an assistant professor and heads the Space and Terrestrial Robotic Exploration (SpaceTREx) Laboratory at the University of Arizona. He is the Engineering PI on the AOSAT I CubeSat Centrifuge mission and is a Co-Investigator on SWIMSat, an Airforce CubeSat mission concept to monitor space threats*